



RNA nanotherapeutics with fibrosis overexpression and retention for MASH treatment

Received: 11 January 2024

Accepted: 7 August 2024

Published online: 27 August 2024

Check for updates

Xinzhu Shan^{1,2,14}, Zhiqiang Zhao^{1,2,3,14}, Pingping Lai⁴, Yuxiu Liu⁵, Buyao Li², Yubin Ke⁶, Hanqiu Jiang¹⁰, Yilong Zhou⁷, Wenzhe Li¹⁰, Qian Wang¹, Pengxia Qin², Yizhe Xue², Zihan Zhang², Chenlong Wei², Bin Ma^{1,2}, Wei Liu⁸, Cong Luo³, Xueguang Lu⁹, Jiaqi Lin¹⁰, Li Shu¹¹, Yin Jie⁵, Xunde Xian⁴, Derfogail Delcassian¹⁰, Yifan Ge¹¹ & Lei Miao^{1,2,13}

Metabolic dysfunction-associated steatohepatitis (MASH) poses challenges for targeted delivery and retention of therapeutic proteins due to excess extracellular matrix (ECM). Here we present a new approach to treat MASH, termed “Fibrosis overexpression and retention (FORT)”. In this strategy, we design (1) retinoid-derivative lipid nanoparticle (LNP) to enable enhanced mRNA overexpression in fibrotic regions, and (2) mRNA modifications which facilitate anchoring of therapeutic proteins in ECM. LNPs containing carboxyl-retinoids, rather than alcohol- or ester-retinoids, effectively deliver mRNA with over 10-fold enhancement of protein expression in fibrotic livers. The carboxyl-retinoid rearrangement on the LNP surface improves protein binding and membrane fusion. Therapeutic proteins are then engineered with an endogenous collagen-binding domain. These fusion proteins exhibit increased retention in fibrotic lesions and reduced systemic toxicity. *In vivo*, fibrosis-targeting LNPs encoding fusion proteins demonstrate superior therapeutic efficacy in three clinically relevant male-animal MASH models. This approach holds promise in fibrotic diseases unsuited for protein injection.

Metabolic dysfunction-associated steatohepatitis (MASH) is a chronic liver inflammation that can progress to fibrosis and cancer, affecting ~5% of the population, causing significant mortality worldwide^{1,2}. Currently, there are limited therapies for the treatment of MASH due

to challenges with delivering to, and treating, the fibrotic micro-environment in the liver³. Inspired by the success of glucagon-like peptide 1 (GLP-1) in diabetes treating, protein-based therapies hold promise for MASH treatment^{4,5}. In animal models of chronic liver

¹State Key Laboratory of Natural and Biomimetic Drugs, School of Pharmaceutical Sciences, Peking University, Beijing, China. ²Beijing Key Laboratory of Molecular Pharmaceutics, School of Pharmaceutical Sciences, Peking University, Beijing, China. ³Department of Pharmaceutics, Wuya College of Innovation, Shenyang Pharmaceutical University, Shenyang, China. ⁴Institute of Cardiovascular Sciences and State Key Laboratory of Vascular Homeostasis and Remodeling, School of Basic Medical Sciences, Peking University, Beijing, China. ⁵Chinese Institute for Brain Research, Beijing, China. ⁶China Spallation Neutron Source, Institute of High Energy Physics, Chinese Academy of Science, Dongguan, China. ⁷Department of Surgery, Nantong Tumor Hospital, Tumor Hospital Affiliated to Nantong University, Nantong, China. ⁸Keymed Biosciences (Chengdu) Limited, Chengdu, Sichuan, China. ⁹Key Laboratory of Colloid, Interface and Chemical Thermodynamics, Institute of Chemistry, Chinese Academy of Sciences, Beijing, China. ¹⁰MOE Key Laboratory of Bio-Intelligent Manufacturing, School of Bioengineering, Dalian University of Technology, Dalian, China. ¹¹Interdisciplinary Research Center on Biology and Chemistry, Shanghai Institute of Organic Chemistry, Chinese Academy of Sciences, Shanghai, China. ¹²Department of Bioengineering, UC Berkeley, Berkeley, CA, USA. ¹³Peking University-Yunnan Baiyao International Medical Research Center, Beijing, China. ¹⁴These authors contributed equally: Xinzhu Shan, Zhiqiang Zhao. e-mail: lmiao_pharm@bjmu.edu.cn

injury, the protein relaxin (RLN) has shown benefits⁶⁻⁸. RLN interacts with the Relaxin Family Peptide Receptor 1 (RXFP1) and inhibits the transforming growth factor-β pathway, which is implicated in fibrosis⁹. Recombinant RLNs are currently undergoing clinical trials for treating heart fibrosis⁸. Other proteins, such as anti-inflammatory cytokines like IL-10, have also been reported to protect mice from liver fibrosis by counterbalancing hyperactive immune responses¹⁰. However, these protein therapies are challenging to translate to the clinics due to limited stability, rapid clearance, and lack of organ targeting specificity.

Strategies to extend protein circulation half-life have been successful for some clinically relevant therapeutic proteins (i.e., IL-2, GLP-1 and etc). Approaches have included protein modifications to introduce the Fc fragment of IgG⁸, PEGylation¹¹, and the addition of long-chain alkanes¹². Yet, this may not be sufficient to enhance drug concentration at the lesion site and could potentially increase systemic toxicity. In parallel, the design of fusion proteins with specific binding domains has been shown to help anchor protein therapeutics in the lesions¹³⁻¹⁵. Unfortunately, the administration of these fusion proteins is mainly limited to local injections in easily accessible disease models, and their manufacturing can be complex and requires further optimization. Therefore, developing strategies for targeted delivery of therapeutic anti-fibrosis proteins and prolonging their retention in fibrotic lesions are critical for MASH treatment.

Lipid nanoparticle (LNP) mRNA therapies have shown enormous promise for expression of nucleic acids encoding for target therapeutic proteins¹⁶. For instance, the RNA drug Onpatro is clinically approved for treating transthyretin-mediated amyloidosis and highlights the therapeutic potential of LNPs for liver diseases. LNPs often preferentially deliver nucleic acid cargo to the liver. This is thought to be due, in part, to adsorption of ApoE proteins to the LNP surfaces, and targeting other organs through chemical modifications to LNPs is an expanding research area^{17,18}.

Although the liver is considered a relatively accessible organ for mRNA LNPs in healthy patients, it becomes less amenable to therapeutic intervention under pathological status of MASH. Once steatosis occurs in metabolic dysfunction, the accompanied steatohepatitis activates hepatic stellate cells (HSCs), which producing an excessive amount of extracellular matrix (ECM). The resulted liver fibrosis often manifests as capillarization and closure of fenestrae, thus restricting drug delivery to the liver¹⁹. The MASH microenvironment is therefore exceptionally challenging for therapeutic delivery of mRNA LNPs.

Here, we present a new strategy for delivering therapeutic proteins to hepatic MASH lesions via mRNA LNPs in a process we term “Fibrosis overexpression and retention (FORT)”. Briefly, we designed a new LNP which incorporates retinoid derivative ligands to facilitate targeted delivery to HSCs. Retinoid derivatives have previously been shown to facilitate fibrotic accumulation of therapeutic regimens due to “attach” to retinol-binding protein-4 (RBP-4)²⁰. Among the analogues tested, carboxylic retinoids, not conventional alcoholic or ester-derived retinoids have shown improved mRNA expression in fibrotic livers. Mechanistic investigations revealed that the carboxylic retinoids rearranged on the outer shell of LNPs during mRNA encapsulation, resulting in improved binding to RBP-4, enhanced internalization, sprouting, and endosomal escape. We use these LNPs to deliver mRNA encoding for engineered proteins which co-express an endogenous peptide domain to “anchor” proteins into the fibrotic ECM. Using this approach, our lead ligand candidate (all-trans retinoic acid, ATRA) demonstrated a ~10-fold increase of mRNA expression in fibrotic livers compared to commercial ALC-0315 formulations. We used this LNP to deliver mRNA encoding for an anti-fibrotic RLN protein fused to an optimized collagen binding domain (CBD) from placenta growth factor (PLGF)^{14,21}. We demonstrate 80% retention of the fusion protein in the liver. We further demonstrate therapeutic reduction in fibrosis in

three clinically relevant MASH models. We believe the FORT approach could be widely applicable to the delivery and anchoring of therapeutic proteins to less accessible fibrotic microenvironment (Fig. 1).

Results

Inclusion of retinoic acid but not retinol improves mRNA delivery to fibrotic livers

We hypothesized that LNP-mediated mRNA expression in the liver would be reduced in models of chronic liver inflammation¹⁷. To test this, we delivered a model mRNA encoding luciferase (mLuc) using clinically-approved LNPs composed of ALC-0315, SM-102 and MC3 in wild type (WT) animals and those with chronic liver inflammation (Fig. 2a-c). mLuc LNPs were administered via intravenous (i.v.) injection to an experimental late-stage liver fibrosis model induced by 6-week administration of tetrachloride (CCl₄) and a MASH hamster model induced by 10-week choline deficient high fat diet (CDHFD) treatment (Fig. 2b, c, Supplementary Figs. 1, 2). We observed a 6-20-fold decrease in mLuc expression delivered by all three types of LNPs in fibrotic models compared to WT controls.

Next, we designed a library of LNPs which would enhance mRNA delivery to HSCs that are known to be abundant in fibrotic livers. Instead of employing a complicated post-fabrication surface modification strategy²², we selected to add an additional component to the LNP which could aid selective accumulation of LNPs in HSCs. HSCs are primarily responsible for retinoid storage²³. In vivo, retinol and selected retinol metabolites bind to the serum protein RBP-4 (Fig. 2d), which then facilitates cellular endocytosis in HSCs²⁰. We therefore developed LNPs containing retinoids and retinoid derivatives spanning four main sub-classes; (I) natural retinols, (II) natural retinol acids, (III) aromatic retinol acids, and (IV) retinol esters (Fig. 2d). These included first generation retinol derivatives which preserved the cyclohexane ring of natural vitamin A, such as retinol, fenretinide and 4-keto-retinol (with a hydroxyl end, group I); ATRA, 13-cis-retinoic acid (13-CRA) and 9-cis-retinoic acid (9-CRA) (with a carboxylic end, Group II), and acetyl retinol (with an ester bond, group IV). We also included a number of second generation of derivatives which had aromatic modifications in the cyclohexane ring area, including acitretin (A-VA) and bexarotene (carboxylic acid derivative, group III), and etretinate (ester derivatives, group IV). The second-generation derivatives have showed selective binding to intracellular retinoid X receptor or retinoid acid receptors²⁴. However, the effects of these modifications on RBP-4 binding and uptake is not well understood. We measured the binding of these retinoid derivatives to RBP-4 (Supplementary Table 1). Most of the first-generation retinoids exhibited high binding affinity ($K_d = 0.5\text{-}5 \mu\text{M}$), consistent with previous report²⁵, while the second generation showed moderate binding ($K_d = 30\text{-}60 \mu\text{M}$).

Based on these findings, we incorporated all retinoid derivatives into LNP formulations containing ALC-0315 as the ionizable cationic lipid. Retinoid derivatives could be directly incorporated into the lipid bilayer of LNPs due to the hydrophobic cyclohexane/aromatic ring and alkene chains (Fig. 2d)²⁶. Retinol derivatives were included at 5 mol% to 25 mol% within the cholesterol component, other original lipid ratio was maintained (Supplementary Data file 1). We evaluated the transfection efficiency of mRNA encapsulated LNPs in activated HSCs (aHSCs, using LX-2 cell line as model) and primary hepatocytes (both WT and lipid-overload). Results shown in Fig. 2e indicate that incorporating carboxylic acid retinol derivatives, as opposed to alcohol or ester derivatives, significantly enhanced mRNA delivery in aHSCs (Supplementary Fig. 3). Notably, ATRA, 13-CRA, and 9-CRA showed a dose-dependent increase in expression, with 5.4-, 4.1- and 4.2-fold increase of expression in aHSCs at 25 mol% incorporation, respectively. The acidic aromatic derivative A-VA and bexarotene showed 5.3- and 4.7-fold increase of mRNA delivery in aHSCs and plateaued at lower incorporation levels (~15 mol%). However, alcohol derivatives (retinol, fenretinide, and 4-keto-retinol) and ester derivatives showed

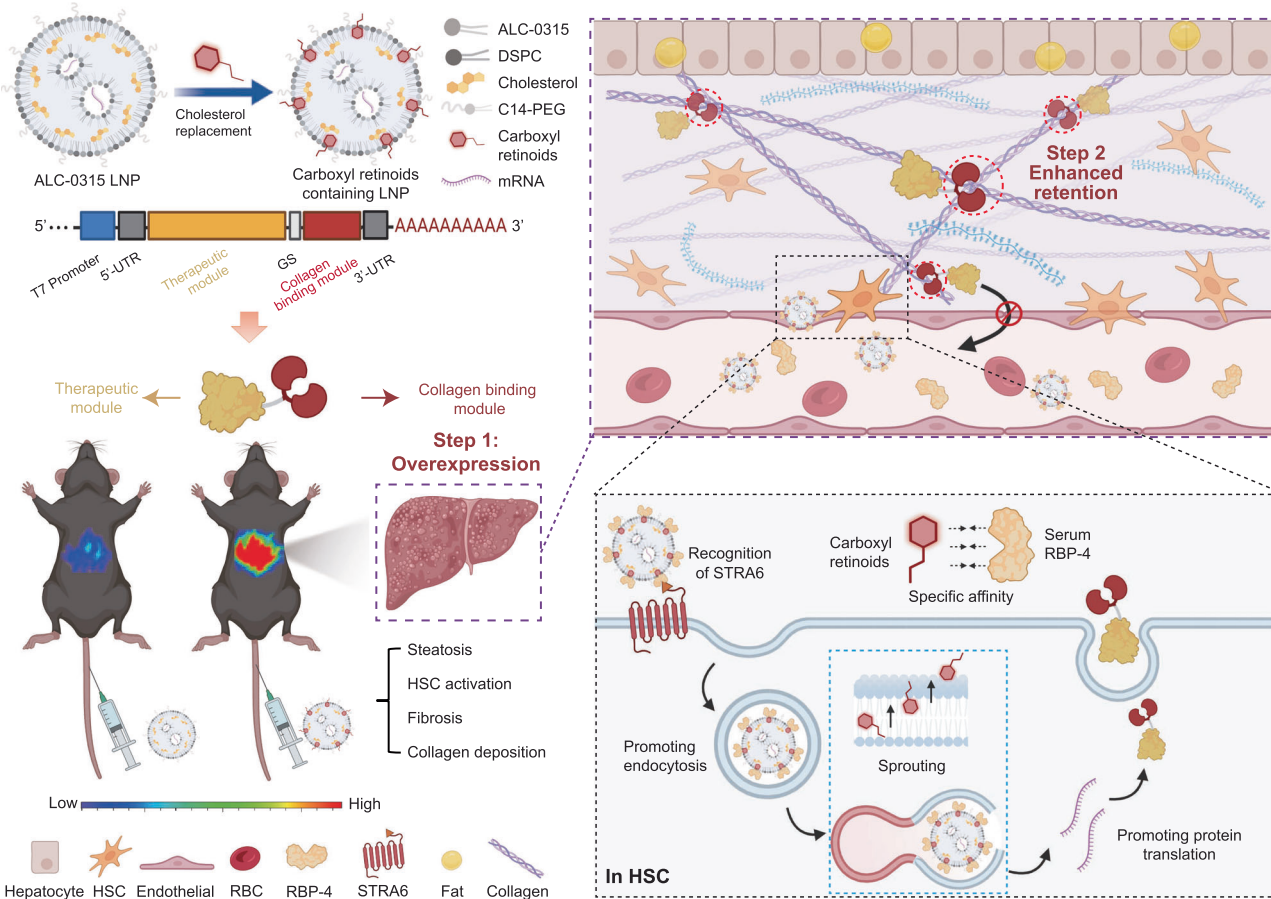


Fig. 1 | Schematic illustration of fibrosis overexpression and retention (FORT) strategy for metabolic dysfunction-associated steatohepatitis (MASH) treatment. Collagen binding domain (CBD) screened from the endogenous proteins was added to the C terminus of RLN with connection of Glycine-Serine linker (GS) and coded by mRNA. The therapeutic recombinant mRNAs were encapsulated with a fibrosis-targeted LNP and intravenously (i.v.) administrated for enhanced mRNA expression and fibrotic liver retention. To achieve enhanced mRNA expression, we fabricated a five component LNPs by substituting 25 mol% of cholesterol in ALC-0315 LNPs with a carboxylic retinoid, all-trans retinoic acid (ATRA), which shows over a ~10-fold increase in mRNA expression compared to traditional ALC-0315

LNPs in fibrotic and MASH models. Mechanistically, the carboxylic retinoid rearranges on LNPs surfaces during encapsulating mRNA, improving both endocytosis and endosomal release. The added CBD to the therapeutic proteins further extended liver retention. Thereby, the FORT strategy allows the fusion protein to be expressed and anchored in situ, creating a depot that enhances the anti-fibrotic response. GS Glycine-Serine linker, HSC hepatic stellate cell, RBC red blood cell, STRA6 stimulated by retinoic acid 6 (a surface receptor for transported retinoids). Figure 1 was created with BioRender.com released under a Creative Commons Attribution-NonCommercial-NoDerivatives 4.0 International License (CC BY-NC-ND 4.0).

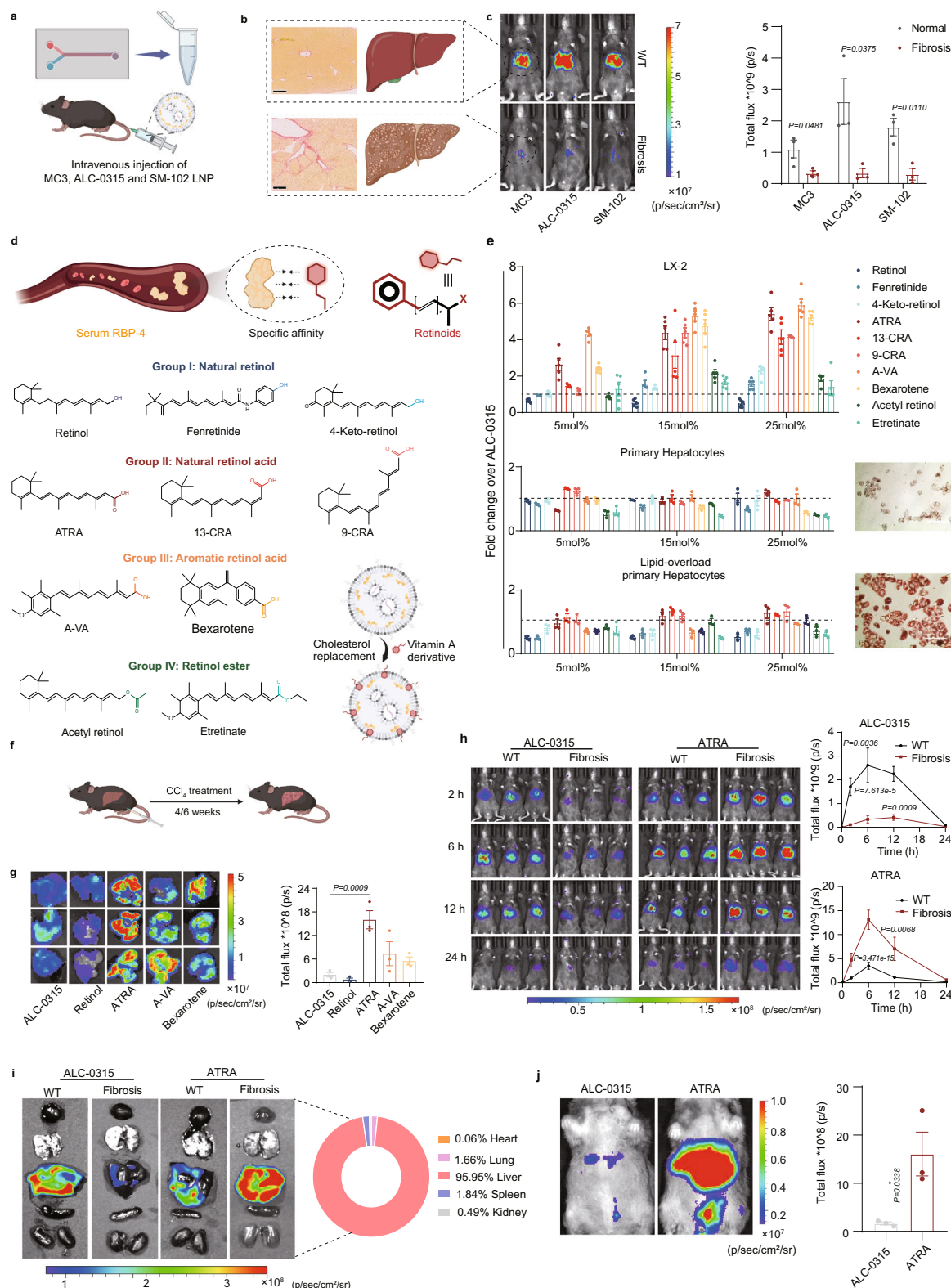
comparable or decreased mRNA expression in aHSCs as compared to the original ALC-0315 formulation. Enhanced protein expression was not observed in healthy or fatty primary hepatocytes treated with retinoid derivative LNPs (RD-LNPs).

To validate these trends *in vivo*, RD-LNPs containing ATRA, bexarotene, A-VA, and retinol (all at a 25 mol% replacement of cholesterol, Supplementary Data file 1) were formulated and compared to control ALC-0315 LNPs. The particle sizes of all five formulations were around 100 nm, with a polydispersity index below 0.1. They exhibited encapsulation efficiency over 70% and a slightly negative charge (Supplementary Fig. 4, Supplementary Table 2). We injected these particles into mice that were pre-treated with CCl₄ for 4 weeks. We observed that ATRA, A-VA, and bexarotene LNPs significantly improved luciferase expression in fibrotic liver rather than the retinol LNPs, with ~8.0-, 3.7- and 2.8-fold increase in luciferase expression compared to the original ALC-0315 formulation in fibrotic livers, respectively (Fig. 2f, g, Supplementary Fig. 5). This observation aligned with the *in vitro* transfection study conducted in LX-2 cells (Fig. 2e), highlighting the potential of targeting aHSCs for LNP delivery in fibrotic livers.

In light of the escalating challenges associated with delivery barriers during the progression of fibrosis, we proceeded to test the efficacy of ATRA LNPs, our optimized formulation, in mice exhibiting

fibrosis induced by 6 weeks of CCl₄ treatment. ATRA LNPs enhanced protein expression ~10-fold compared to the ALC-0315 formulations, however this increased expression was not observed in WT mice (Fig. 2h). Over 95% of mRNA was expressed in liver rather than other organs (Fig. 2i, Supplementary Fig. 6). The same trend was also observed in an MC3 formulation containing ATRA, demonstrating the universal effectiveness of carboxylic RD-LNPs, particularly ATRA, in facilitating LNP delivery to fibrotic livers (Supplementary Fig. 7). We also investigated the biodistribution of ATRA LNPs and ALC-0315 LNPs by intravenously injecting CCl₄-treated mice with 1,1-dioctadecyl-3,3,3,3-tetramethylindotricarbocyanine iodide (DiR)-labeled ATRA and ALC-0315 LNPs. Quantification of the fluorescence signal indicated that ATRA LNPs exhibited higher and more specific distribution in the liver compared to ALC-0315 LNPs, with over 94% of LNPs accumulating in the liver (Supplementary Fig. 8). Consequently, the enhanced protein expression observed with ATRA LNPs correlated with the increased accumulation in the fibrotic liver.

Finally, we established a hamster CDHFD-induced MASH model as a more clinically relevant system. We then compared luciferase expression in these hamsters treated with ATRA-containing mLuc LNPs via jugular vein injection, or standard ALC-0315 mLuc formulations. Results were similar to CCl₄ treated mice:



we observed a 9.7-fold increase in expression in MASH hamster liver when ATRA was added to the original LNP formulations (Fig. 2j, Supplementary Fig. 9). Together, these data demonstrate improved LNP delivery and mRNA translation to fibrotic liver *in vitro* and *in vivo* through incorporation of carboxylic retinoids in the LNP formulations.

Rearrangement of retinoic acid in LNP facilitates endocytosis and endosomal release of RNA in aHSCs

To validate the role of aHSCs in mediating enhanced mRNA expression in fibrotic livers treated with RD-LNPs, we looked mRNA encoded protein expression in CCl₄ treated *tdTomato* reporter mice (C57BL6/J background) (Fig. 3a). Following the induction of fibrosis, we

Fig. 2 | Incorporation of carboxylic retinoids in LNPs increased mRNA expression in HSCs and fibrotic livers. **a–c** Comparison of mRNA expression delivered by representative LNP formulations in wild type (WT) livers and tetrachloride (CCl_4) treated fibrotic livers 6 h after i.v. injection. mRNA encoding luciferase (mLuc) was used as reporter mRNA, 0.25 mg/kg in LNP formulations were administered, $n = 3$ mice. **d** Structures of different groups of retinoid derivatives incorporated into original LNP formulation as a partial substitution of cholesterol. **e** In vitro expression of mRNA delivered by retinoid derivative LNPs (RD-LNPs) formulations in LX-2 cells, primary hepatocytes and lipid-overload primary hepatocytes. Twenty-four hours after incubation of 70 ng mRNA LNPs, the expression was measured using plate reader. Expression fold changes over ALC-0315 formulations were calculated and presented ($n = 5$ in LX-2 cell line, $n = 3$ in hepatocytes.). Brightfield images show the morphology of WT (middle) and lipid over-load (bottom) primary hepatocytes, scale bar represents 100 μm . **f** Schematic illustration of CCl_4 induced liver fibrosis

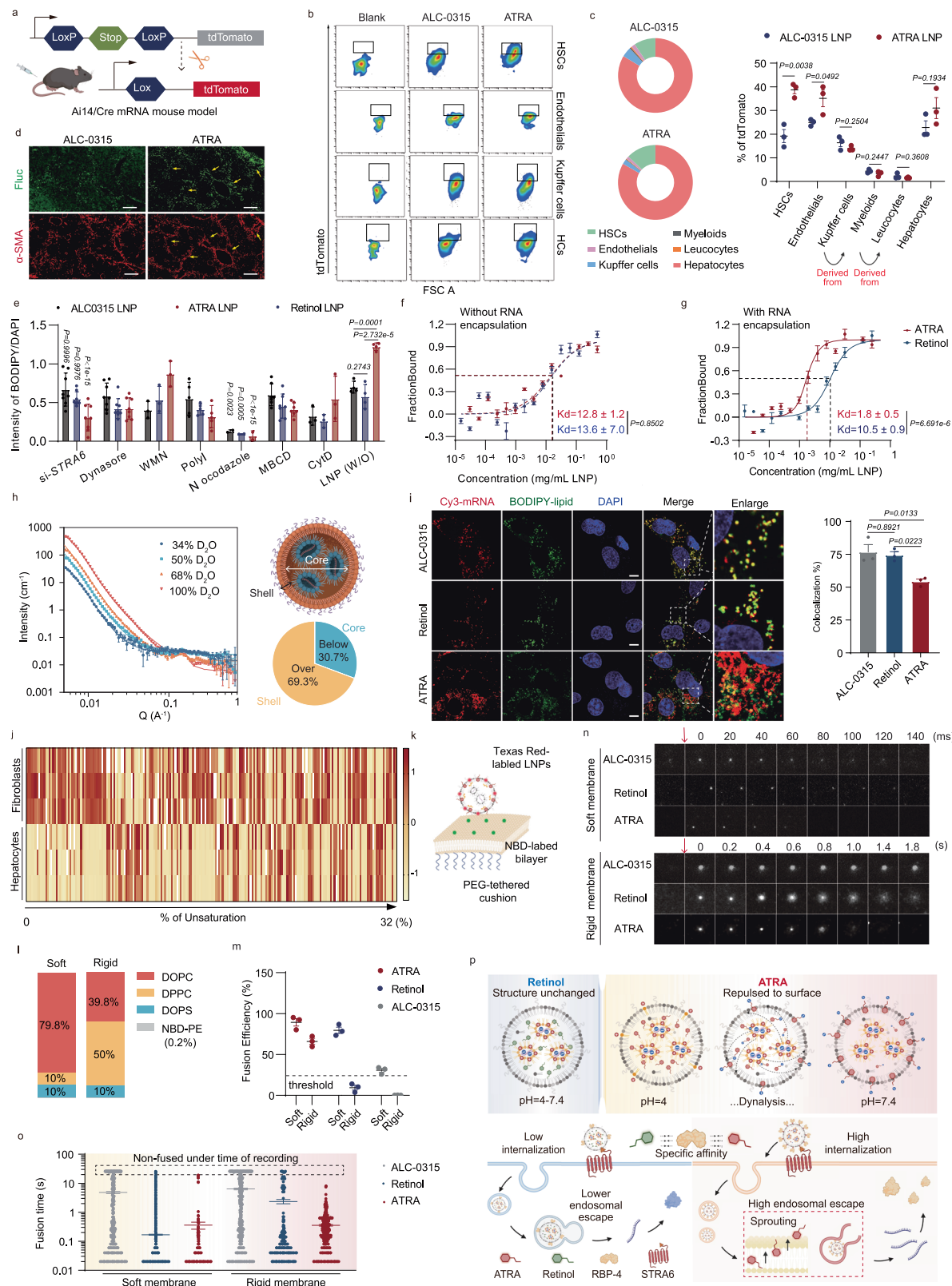
mice model. **g** Expression of mLuc 24 h after i.v. injection of the representative RD-LNPs and the original ALC-0315 LNPs (0.25 mg/kg, $n = 3$ mice). Quantification of the expression was presented on the right. **h, i** The mRNA expression kinetics delivered by the original ALC-0315 formulation and 25% ATRA formulations were compared in CCl_4 -treated (6 week) fibrosis mice. Expression was measured by In Vivo Imaging System at multiple time points after injection. Quantification was presented on the right (0.25 mg/kg, $n = 3$ mice). **j** Comparison of expression between the original ALC-0315 and ATRA formulations in hamster MASH models at a dose of 0.25 mg/kg. The expression was measured at 6 h after injection, $n = 3$ mice, one representative animal from each group were listed. Data were represented as mean \pm SEM. Statistical significance was calculated through two-tailed unpaired Student's *t*-test (**c, j**). One-way ANOVA with Dunnett test (**g**) and Two-way ANOVA with Sidak test (**h**). Figure 2a, b, d and f were created with BioRender.com released under CC BY-NC-ND 4.0. Source data are provided as a "Source Data" file.

administered LNPs encoding for cre-recombinase mRNA (mCre LNPs). The tdTomato mice carry a LoxP flanked stop cassette mutation, and upon expression of Cre, the cells express tdTomato (Fig. 3a). We used flow cytometry to quantify the transfection efficiency of ALC-0315 LNPs and ATRA LNPs in different cells within the fibrotic livers. No significant difference was observed in the expression of tdTomato in the leucocyte population. However, ~40%, over twofold increase in the number of tdTomato^+ cells were observed in HSC-like population treated with ATRA LNPs compared to those treated with ALC-0315 LNPs (Fig. 3b, Supplementary Fig. 10). This result aligns with the in vitro study and suggests that ATRA LNPs tend to accumulate in the fibrotic area (Fig. 3c). Furthermore, we evaluated the co-localization of luciferase and alpha-smooth muscle actin (α -SMA), a marker for fibrosis, using immunofluorescence (IF) staining. Consistently, results revealed that the majority of the expressed luciferase was localized within the α -SMA $^+$ fibrotic areas in mice treated with ATRA LNPs (Fig. 3d). To visualize the distribution of LNPs within the liver, we labeled the LNPs with DiR. The results demonstrated that compared to ALC-0315 LNPs, a significant proportion of ATRA LNPs exhibited a tendency to accumulate within the α -SMA $^+$ fibrotic regions (Supplementary Fig. 11) surrounding the blood vessels. These findings confirm the unique ability of ATRA-modified LNPs to achieve enhanced delivery and express the encapsulated protein specifically in fibrotic areas. In addition to stromal cells, we also observed a slight but not significant increase in the expression of tdTomato in hepatocytes following treatment with ATRA LNPs (Fig. 2c). This suggests that ATRA LNPs penetrated the parenchyma and improve expression of hepatocytes, potentially due to the improved uptake of vitamin A in hepatocytes during the progression MASH^{27–29}. However, the mechanisms underlying the improved uptake of hepatocytes require further investigation.

We next investigated the rationale of acidic retinoid derivatives in facilitating mRNA delivery to HSCs. BODIPY-labeled LNPs were used to assess cellular uptake through high-content microscopy (for LX-2 HSCs) and flow cytometry (for primary hepatocytes). The transfection time was limited to 1.5 h to avoid non-specific lipofection that is often observed with longer incubation time. To explore the potential mechanisms of endocytosis, the cells were treated with small-molecule inhibitors of clathrin/caveolae-mediated endocytosis and macropinocytosis prior to LNP treatment (Fig. 3e, Supplementary Fig. 12). Specifically, ATRA and A-VA LNPs showed 1.5–2-fold higher uptake compared to ALC-0315 LNPs in ahSCs (LX-2 cells). Retinol, Acetyl-Retinol, and Etretinate LNPs exhibited slightly lower but comparable uptake to ALC-0315 LNPs. In contrast, ATRA did not significantly facilitate LNP uptake in both WT and fatty hepatocytes (Supplementary Fig. 12). Macropinocytosis was identified as a major pathway for LNP uptake for all LNPs tested, consistent with previous reports^{30,31}. In a separate study, we also knocked down the gene of RBP-4 receptor STRA6 with siRNA 24 h prior to adding LNPs (Supplementary Fig. 13) in ahSCs. Interestingly, knockdown of STRA6 significantly reduced the

uptake efficiency of retinoic acid LNPs (ATRA and A-VA LNPs) by approximately 2–3-fold in ahSCs. A light, non-significant decrease was observed in the retinol or retinol-ester groups (Acetyl Retinol and Etretinate LNPs). In contrast, STRA6 did not significantly affect hepatocytes uptake of ATRA LNPs (Supplementary Fig. 14). This suggests that only the acidic retinoid derivative LNPs significantly rely on STRA6 for enhanced endocytosis in ahSCs. To further examine whether the interaction between RBP-4 and STRA6 facilitate the endocytosis of retinoic acid LNPs in LX-2 cells, we supplemented the cells with additional RBP-4 protein. This led to a slight but significant increase in the ATRA LNP-treated groups, further supporting the role of acidic retinoid in enhancing LNP binding to HSCs through the RBP-4 -STRA6 pathway (Supplementary Fig. 12). We then used MicroScale Thermo-phoresis (MST) to measure the binding affinity between RBP-4 protein and mRNA loaded or empty LNPs. As expected, ALC-0315 LNP without added retinoids did not bind with RBP-4 protein (Supplementary Fig. 15); however, the addition of retinoids improved LNP binding to RBP-4. Interestingly, encapsulating mRNA into retinol LNPs did not change the binding affinity, whereas adding of mRNA into ATRA LNPs led to approximately a 10-fold increase in the binding affinity with RBP-4 (Fig. 3f, g). This suggests lipid organization in ATRA LNPs is altered following the encapsulation of mRNA. We hypothesized that it could be due to charge-mediated repulsion and lipid re-arrangement during LNP assembly. Briefly, the carboxylic acid derivative has a pKa around 4–5 (Supplementary Table 1). During LNP synthesis and dialysis, the pH switches from 4 to 7. Consequently, the retinoic acidic derivative could be rearranged into the LNP surface to minimize negative charge interactions between the negatively charged mRNA and carboxylic acid derivative. This would make the carboxylic acid more accessible to RBP-4, impacting binding affinity and the associated endocytosis pathways. To gain further insights into the LNP structure, we employed Small-Angle Neutron Scattering (SANS) as previously described^{16,32}. The distribution of the ATRA within LNPs was elucidated by varying the content of deuterated water (D_2O) to match the scattering length densities of different region of the particle (Supplementary Tables 3–5). Using a core-shell particle model to fit the SANS data, the results suggested that at least 70% of deuterium-labeled ATRA was preferentially located in the outer shell region, supporting our hypothesis (Fig. 3h).

Adding exogenous RBP-4 to cell culture medium only slightly increased mRNA expression in cells treated with ATRA LNPs, indicating that other mechanisms may mediate the enhanced expression of mRNA. We next looked into the endosomal release kinetics of mRNA LNPs. We labeled LNPs with BODIPY-lipid and Cy3-mRNA and tracked the intracellular transport of LNPs using confocal microscope via an Airyscan detector unit. We observed a significant dissociation of mRNA from dye-labeled LNP 2 h post uptake in LX-2 cells (Fig. 3i), suggesting rapid disassembly and release of mRNA from endosomes in cells treated with ATRA LNP group. In contrast, around 80% of mRNA was still co-localized with LNPs in other groups. To understand the



accelerated lipid-dissociation and mRNA release in more detail, we isolated the endosome compartment from activated fibroblasts and hepatocytes and performed lipidomic analysis (Fig. 3j, Supplementary Data file 2 and 3, Supplementary Figs. 16–20). The result of lipidomics revealed that hepatocytes' endosome has a lower saturation lipid content compared to HSCs', suggesting that HSCs possess more rigid endosomal membranes. To mimic different properties on membrane

packing, we created polymer-tethered lipid bilayer system using simplified lipid components, i.e., with 1,2-Dioleoyl-sn-glycero-3-phospho-L-serine (DOPS) providing the net negative charge, 1,2-dioleoyl-sn-glycero-3-phosphocholine (DOPC) and 1,2-Dipalmitoyl-sn-glycero-3-phosphocholine (DPPC) constituting the main bilayer structures (Fig. 3k, Supplementary Table 6)³³. The ratio of DOPC and DPPC was tuned to match the saturation levels of the endosomal membranes

Fig. 3 | Mechanisms of the improved mRNA expression of ATRA LNPs. **a** mCre delivery activates tdTomato expression. The mice were treated with CCl₄ for 4 weeks before LNPs dosing. **b** Representative FACS analysis of tdTomato⁺ cells in different cells within fibrotic livers. Three mice were dosed mCre LNPs 48 h before sacrifice. **c** Quantification of tdTomato⁺ cells in cell population ($n=3$). **d** Representative staining of luciferase and α -smooth muscle actin (α -SMA) after dosing with mLuc LNPs in fibrotic livers. Scale bar: 100 μ m. Experiments were repeated three times independently with similar results. **e** Cellular internalization of LNPs with inhibition of various internalization pathways. LNP(W/O): $n=4$; siSTR4 and dynasore: $n=8$; MBCD: $n=7$; poly I: $n=5$; WMN and CytD: $n=3$; nocodazole: $n=2$. Dose-response curve for the interaction between LNPs and RBP-4 protein. $n=5$ in (f), $n=5$ for Retinol, $n=3$ for ATRA in (g). **h** Characterization of ATRA distribution within LNPs. Data (symbols) and fit (lines) were presented. The core-shell structure of LNP and the percentage of distribution in inner core and outer shell. **i** Representative confocal images show the release of mRNA (Cy5) from LNPs (BODIPY) ($n=3$). Scale bar: 10 μ m. **j** Z-score heatmap representing relative quantifications of phosphatidyl choline (PC) in the endosomes of hepatocytes and activated fibroblasts (ranked by unsaturation %, $n=3$). **k** Schematic of the lipid bilayer mimicking the endosome membranes. **l** Lipid composition for the mimicked endosomal membrane of hepatocytes and fibroblasts; **m** The fusion efficiency of LNPs with the two membranes ($n=3$). **n** Representative trace of the Texas red labeled LNPs fusing with the mimicked membranes. **o** The recorded fusion time ($n=467$ for ALC-0315; $n=491$ (soft) and 783 (rigid) for ATRA; $n=29,705$ (soft) and 212 (rigid) for retinol). **p** The hypothesis for increased internalization and endosomal escape of ATRA LNPs. Data were represented as mean \pm SEM, “ n ” indicates biologically independent samples. Statistical significance was calculated through two-tailed unpaired Student’s *t*-test (c, f, g) and One-way ANOVA with Tukey test (e, i). Figure 3a, h, k and p were created with BioRender.com released under CC BY-NC-ND 4.0. Source data are provided as a “Source Data” file.

from HSCs and hepatocytes (Fig. 3i). Membrane rigidity was confirmed via measuring the diffusion coefficient using fluorescent correlation spectroscopy (Fig. 3m, n). We used Texas-red phosphatidylethanolamine (PE) labeled LNPs encapsulated mRNA to test the fusion kinetics between the artificial bilayer and LNPs. Interestingly, all three types of LNPs efficiently and rapidly fused within the soft membrane mimicking hepatocyte endosomes, with ATRA exhibiting slightly faster and more complete fusion (>90% fused) (Supplementary Table 7, Fig. 3m, n, Supplementary Video 1). However, in the rigid membrane mimicking HSC endosomes, almost no fusion events were observed for ALC-0315 LNPs (Fig. 3m, n, Supplementary Video 2). Nevertheless, ATRA LNPs exhibited over 50% fusion at the endpoint (Fig. 3m), with faster diffusion compared to other LNP-treated membranes (Fig. 3o). Additionally, the diffusion coefficient of the acceptor artificial membrane was significantly increased after treating with ATRA LNPs, suggesting lipid protrusion and mixing may play a role (Supplementary Fig. 21). Thus, we further proposed that the charge-mediated repulsion of ATRA to the outer shell of LNP might facilitate lipid protrusion and sprouting, ultimately enhancing endosomal escape (Fig. 3p). Overall, these findings enhance our understanding of the mechanisms underlying the improved transfection efficiency observed with retinoic acid LNPs targeting HSCs.

mRNA encoding collagen binding recombinant proteins improved retention in fibrotic region

Following the successful accumulation of mRNA LNPs in HSCs and the site-specific expression of protein in fibrotic liver regions, our next objective was to evaluate the strategy to retain the therapeutic protein in the fibrotic livers. The therapeutic peptide utilized in our study was a peptide hormone relaxin (RLN), with anti-fibrotic effects that has been clinically tested for treating cardiovascular diseases. Based on the previously reported RLN mRNA delivery for fibrosis treatment^{34,35}, we aimed to further anchor this protein in fibrotic lesions in the liver to enhance its local expression (Fig. 4a). Through comparison between RNA levels of WT hamsters and hamsters with MASH, we identified col1 α 1 and col1 α 2 as major ECM proteins significantly increased in MASH livers (Supplementary Fig. 22)³⁶. We decided to add ECM binding domains to the RLN hormone to evaluate if mRNA modifications could be used to enhance protein retention in the fibrotic livers. For initial screening, we chose 11 CBD sequences derived from endogenous proteins such as decorin, fibronectin, osteopontin and others (Fig. 4b)^{37–40}. Naturally occurring RLN is synthesized as a single-chain pro-RLN consisting of a receptor binding B-chain on the N-terminus, an A-chain on the C-terminus that forms disulfide bridges with B-chain to improve its stability, and a connecting C-chain in between. Processing of the pro-RLN to RLN occurs in vivo through the endoproteolytic cleavage of the C-peptide. However, delivering the A and B-chain peptides separately often leads to reduced protein stability

and assembly challenges⁴¹. Therefore, we retained the original mRNA sequence encoding the pro-RLN (Fig. 4a, Supplementary Data file 4). As the B-chain’s two receptor binding sites are crucial for RLN function, we added the CBD peptides adjacent to the A-chain and close to the C terminus. There is low homology between human and mouse RLN and mouse RLN 1 exhibits similar folding and functionality to human RLN 2 which is currently being studied in clinical trials⁴². We therefore designed mouse and hamster RLN 1 fusion proteins tailored to our animal models. To preserve the structure of both RLN and CBD, we incorporated a flexible Glycine-Glycine-Glycine-Serine (GGGS) linker between the CBD and A chain. Pseudo-uridine-modified mRNAs encoding the 12 fusion proteins were prepared using in vitro transcription (Supplementary Fig. 23). These mRNAs were then formulated with the previously screened ATRA LNPs. Cryo-electron microscopy images confirmed the presence of uniformly solid spherical structures of the resultant RLN-CBD mRNA (mRLN-CBD) LNP formulations (Fig. 4c). The expression of LNP delivered mRLN-CBD was confirmed through IF analysis of the fixed cells and enzyme-linked immunosorbent assay (ELISA) of the supernatant. All fusion peptides exhibited similar expression levels, which were comparable to or slightly lower than that of the unmodified RLN peptide (Supplementary Fig. 24). To assess the binding capability of the fusion protein with collagen, we conducted a sandwich ELISA study. We collected supernatant from mRNA-treated cells to quantify the concentration of the secreted protein, and evaluated the binding of the flag-tagged fusion protein to a collagen-coated plate with anti-flag tag antibodies (Fig. 4d). The results demonstrated that the addition of CBD Pep K to RLN led to strong and versatile binding to ECM proteins (Fig. 4e and Supplementary Fig. 25)¹⁴. Pep K is derived from CBDs found in placenta growth factor-2 (PLGF-2₁₂₃₋₁₄₄), and was selected as the CBD domain candidate for the remainder of our study. In addition, it was also found that a scrambled sequence of PLGF-2₁₂₃₋₁₄₄ fused to protein did not show any specific binding to collagen, suggested the specific binding property¹⁴.

RLN-PLGF₁ mRNA delivered by ATRA LNPs showed improved retention and comparable activity in fibrotic livers

To further augment the collagen binding capability of our RLN-CBD fusion protein, we expanded PLGF motifs from 1 to 3 units, creating two new fusion proteins: RLN-PLGF₁ and RLN-PLGF₃, and tested their properties as compared with native RLN and IgG Fc fused RLN known to prolong systemic circulation (Fig. 5a). Molecular modeling and simulations suggested minimal interaction between each fusion domain in RLN-PLGF₁ and RLN-Fc, while RLN-PLGF₃ showed multiple hydrogen bonds which potentially impact the folding of each unit (Fig. 5b, Supplementary Video 3–5). We then constructed mRNA encoding the four proteins (Supplementary Fig. 26). When delivering these mRNAs with ATRA LNPs, RLN-PLGF₃ had lower expression levels

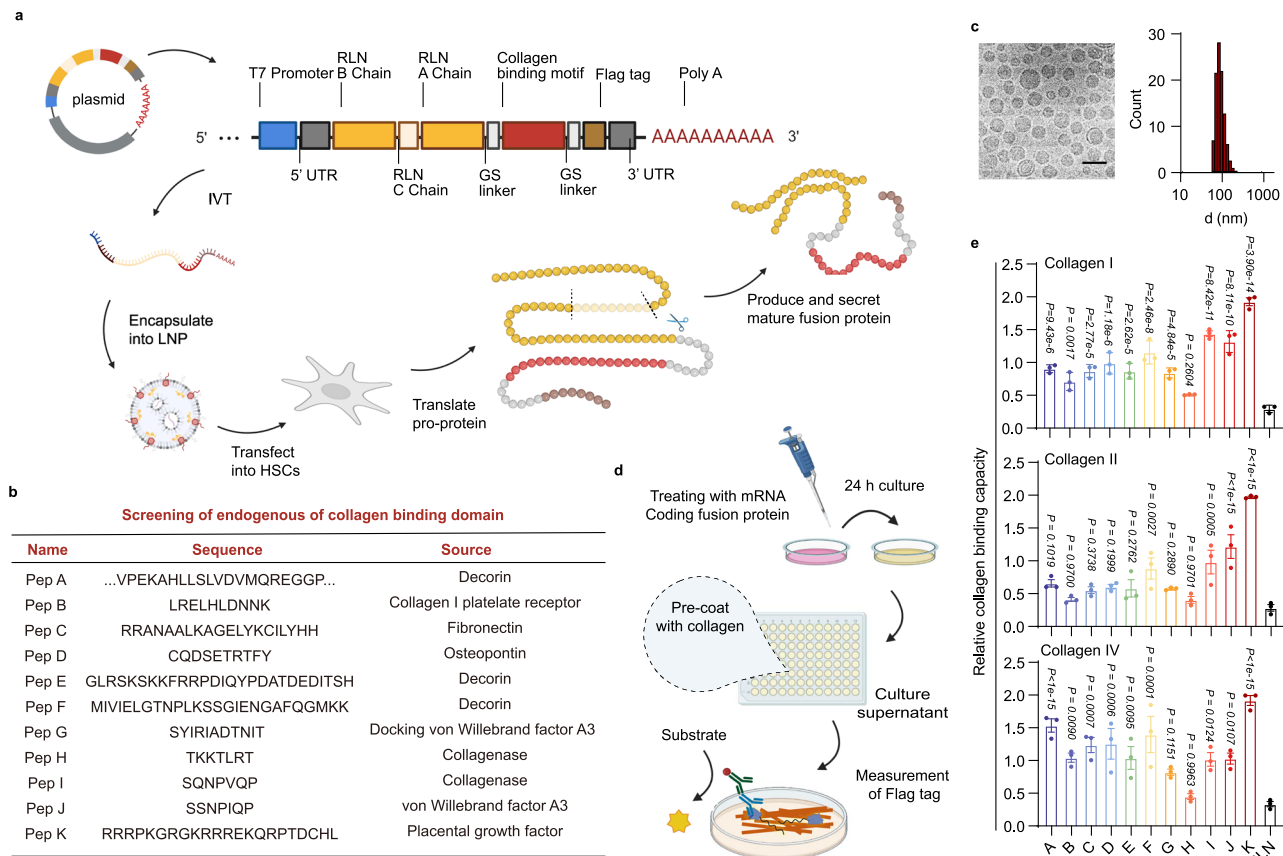


Fig. 4 | Rational design of mRNA encoded RLN-CBD fusion proteins and verification of their ECM binding capacity. **a** Schematic illustration of the structure of mRNA encoded RLN-CBD fusion protein. The ORF encodes the pro-RLN (B, C, A chain) and the CBD domain connected by a flexible GS linker. The mRNA was in vitro transcribed with the linearized plasmid as the template. mRNA was then encapsulated into ATRA LNPs, transfected into HSCs and subsequently expressed the pro-RLN-CBD. The pro-RLN was then processed to a mature secretable RLN-CBD protein; **b** Lists of 11 endogenous CBDs screened in our study. **c** Cryo-electron microscopy and particle size characterization of fusion protein coded mRNA formulated with ATRA LNP (RLN-Pep K LNP for representative), scale bar represents 100 nm. Experiment was repeated three times independently with similar results.

d Schematic illustration for the enzyme-linked immunosorbent assay (ELISA) method used to assess the collagen binding capacity of the fusion proteins expressed from mRLN-CBD LNPs. **e** The binding of RLN-CBD fusion proteins to collagen measured by ELISA. Binding capacity was calculated by absorbance at 450 nm deducted the value of binding to bovine serum albumin (BSA) and further divided with the concentration of proteins in the supernatant ($n = 3$ independent experiments, mean \pm SEM). Statistical significance was calculated through one-way ANOVA with Dunnett's multiple comparison test. Figure 4a and d were created with BioRender.com released under CC BY-NC-ND 4.0. Source data are provided as a "Source Data" file.

compared to the other three proteins (Fig. 5c and Supplementary Fig. 27). This reduced expression was likely due to the hindrance of folding and secretion caused by the hydrogen bonds. Additionally, RLN-PLGF₃ did not improve collagen binding capability (Fig. 5d). In comparison, RLN-PLGF₁ demonstrated improved collagen binding over RLN-PLGF₃, RLN and RLN-Fc, and was considered as the optimized lead RLN-CBD. We then purified RLN, RLN-PLGF₁ and RLN-Fc, and determined their K_d values against collagen II using surface plasmon resonance (SPR). Results showed a relatively high binding affinity with ~20 nM of K_d value for the RLN-PLGF₁ fusion protein. In contrast, unmodified RLN and RLN-Fc did not exhibit significant binding to collagen II (Fig. 5e).

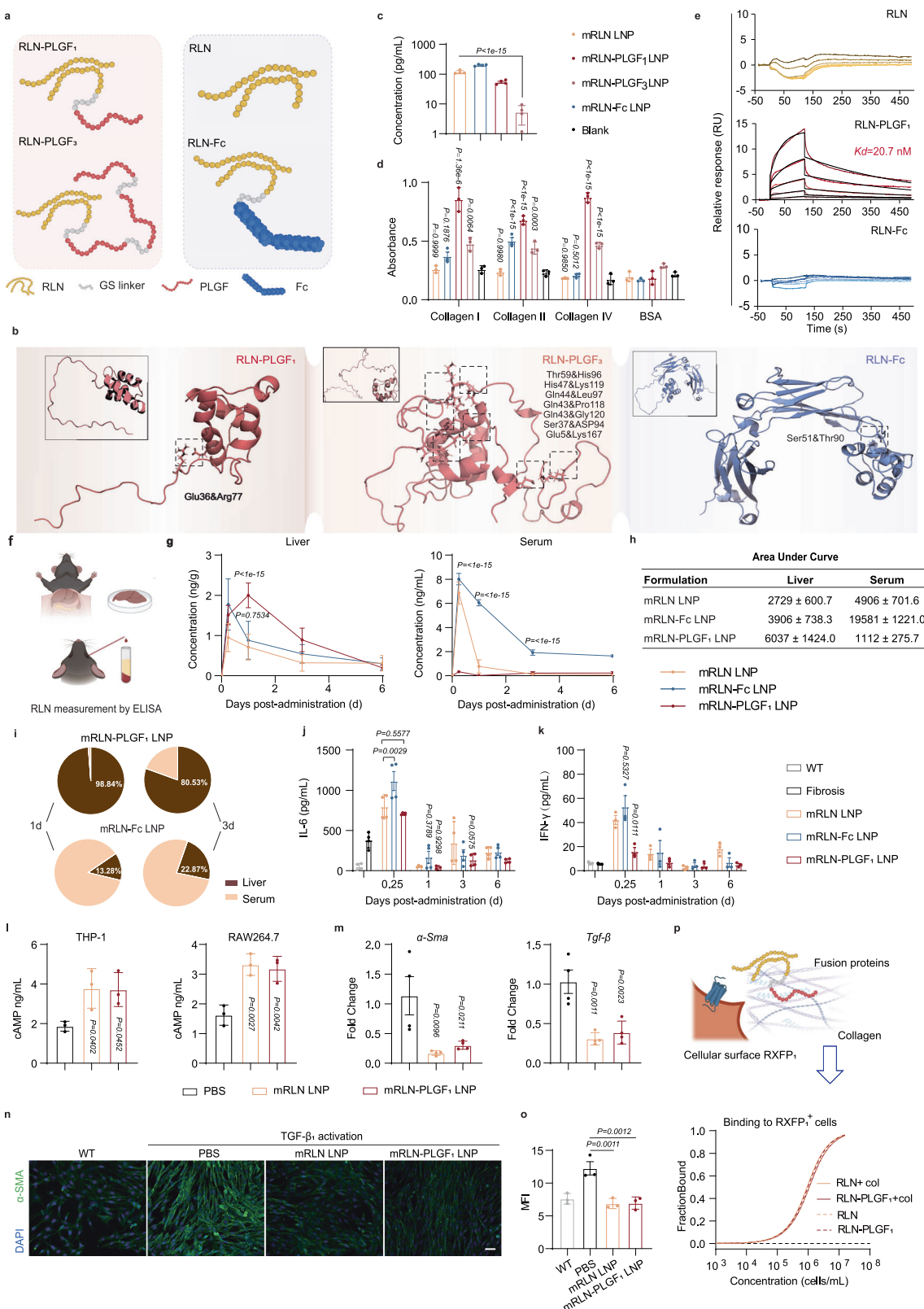
To explore the protein retention in vivo, we delivered 1.5 mg/kg of each of the three mRNA to CCl₄-treated mice using ATRA LNPs (1.5 mg/kg) (Fig. 5f). RLN-PLGF₁, but not RLN-Fc, improved the accumulation of RLN within the liver (Fig. 5g, h). The AUC of RLN in mRLN-PLGF₁ group was ~2 times higher than mRLN-Fc and 3 times higher than unmodified RLN (Fig. 5g, h). Notably, RLN-Fc exhibited prolonged systemic circulation, while minimal RLN-PLGF₁ was detected in the blood during sample collection (Fig. 5g, h). Three days post-injection, over 80% of RLN-PLGF₁ was retained in the liver, whereas ~80% of RLN-Fc were circulated in the bloodstream (Fig. 5i).

Immunofluorescence staining revealed that the majority of RLN-PLGF₁ was expressed and anchored around the α -SMA⁺ fibrotic areas, whereas the free RLN was primarily disseminated or cleared 24 hours after the intravenous delivery of mRNA LNPs (Supplementary Fig. 28).

Both free RLN and RLN-Fc showed significantly higher levels of inflammatory cytokines (e.g., IL-6, IFN- γ) within 6 days of injection compared to RLN-PLGF₁, confirming systemic toxicity was reduced using the RLN-PLGF₁ modality (Fig. 5j, k and Supplementary Fig. 29).

The biological activities of the recombinant proteins were measured using a cAMP activation assay. Both mRLN and mRLN-PLGF₁ encoding fusion proteins activated cAMP (Fig. 5l). The fusion proteins were able to inhibit α -Sma and Tgf- β expression, key proteins regulated by RLN to control fibroblast activation, at both the mRNA and protein levels (Fig. 5m–o).

RLN acts through the RXFP1 receptor⁴². MST assays were performed to examine if RLN to RXFP1 binding were negatively impacted using the collagen-anchored RLN-PLGF₁ (Fig. 5p and Supplementary Fig. 30). Cell lysates from 293F cells containing free RLN-His-tag protein and RLN-PLGF₁-His-tag protein were incubated with collagen IV at the saturation concentration. RXFP1⁺/RXFP1⁻



cells were then incubated with free and collagen-treated RLN-His-tag protein and RLN-PLGF₁-His-tag protein. The addition of collagen did not significantly affect the binding of RLN-PLGF₁ to RXFP1⁺ cells. No significant binding was observed for RXFP1⁻ cells (Supplementary Fig. 30). Collectively, these findings demonstrate that the fusion of RLN with 1 unit of the PLGF domain facilitates collagen anchoring whilst maintaining RLN function.

mRLN-PLGF₁ in ATRA LNPs reduces fibrosis and fatty liver in a CCl₄-treated fibrosis and (methionine/choline deficient) diet induced MASH models

We assessed the anti-fibrosis effect of the FORT strategy in CCl₄-induced liver fibrosis mouse models (Fig. 6a). Four doses of ATRA LNPs containing different mRNA constructs (encoding RLN, RLN-PLGF₁, and RLN-Fc) or empty LNPs were i.v. administrated to CCl₄-

Fig. 5 | mRLN-PLGF₁ formulated in ATRA LNPs showed enhanced retention with preserved bio-activity. **a** Schematic representations of fused and un-modified RLN. **b** The predicted molecular models and dynamic simulations of fused and un-modified RLN. **c** RLN and fusion proteins levels in the supernatant of HSCs transfected with mRNA ATRA LNPs, measured by ELISA of mouse RLN ($n = 4$). **d** The binding of fused and un-modified RLN to collagens as measured by ELISA, with the binding to bovine serum albumin as control ($n = 3$). **e** Affinity of fused and un-modified RLN against collagen II. The fitted Kd values are shown. **f** Schematic representation of the pharmacokinetics of RLN after i.v. administration of ATRA mRNA LNPs. Liver and blood were harvested at multiple time points after mRNA LNP treatment. **g** Kinetics of mRNAs-encoded fused and un-modified RLN in liver and blood (1.5 mg/kg, $n = 5$). **h** The area under curve of (g). **i** Allocation ratio of expressed RLN-PLGF₁ and RLN-Fc in liver and blood 1 day and 3 days post treatment. Systemic levels of inflammatory cytokines at different times after LNP

treatment, $n = 4$ mice in (j) and $n = 3$ mice in (k). **j** Cyclic AMP (cAMP) levels in THP-1 and RAW264.7 cells 12 h after fused and unmodified mRLN LNP treatment (1 μ g mRNA/mL, $n = 3$). **m** Relative mRNA expression of α -Sma and $Tgfb\beta$ in 3T3 cells 24 h after treatment of mRLN or mRLN-PLGF₁ LNPs (1 μ g mRNA/mL, $n = 4$). **n, o** Representative staining and quantification of α -SMA 48 h after fused and unmodified RLN mRNA LNPs treatment (1 μ g mRNA/mL). Scale bar represents 20 μ m ($n = 3$ independent experiments with similar results). **p** Dose-response curve for the interaction between RLN or RLN-PLGF₁ and 3T3 cells with and without collagen IV (fitted from 3 independent experiments in Supplementary Fig. 30). Data were presented as mean \pm SEM, “ n ” indicates biologically independent samples. Statistical significance was calculated through One-way ANOVA with Dunnett test (c, d, l–o), Two-way ANOVA with Sidak test (g, j, k). Figure 5a, f and p were created with BioRender.com released under CC BY-NC-ND 4.0. Source data are provided as a “Source Data” file.

treated mouse. As a positive control, we also orally administered obeticholic acid (OCA), a clinically investigated small molecule for treating MASH (Fig. 6a)²⁶. OCA reduced liver index and collagen deposition (Fig. 6b–f), leading to a decrease in MASH severity. However, its effect on serum alanine transaminase (ALT) and aspartate transaminase (AST) was minimal (Fig. 6b). This is consistent with clinical observations in humans.²⁷ ATRA LNPs containing mRLN moderately reduced liver fibrosis index and AST/ALT levels. In contrast, mRLN-Fc LNPs, which extended the systemic circulation, showed enhanced therapeutic improvement compared to mRLN LNPs. However, mRLN-Fc LNPs showed systemic toxicity with significant weight loss (Supplementary Fig. 31). Notably, treatment with mRLN-PLGF₁ LNPs demonstrated the most significant benefits in reversing liver fibrosis. It led to a ~13% decrease in liver index, normalized AST/ALT, 6.4-fold reduction in α -SMA expression, 4.3- and 6.7-fold decrease in Masson's trichrome and Sirius red staining, more pronounced than the positive control OCA group (Fig. 6b–g). Hematoxylin-eosin (H&E) staining also revealed reduced liver damage (Fig. 6h).

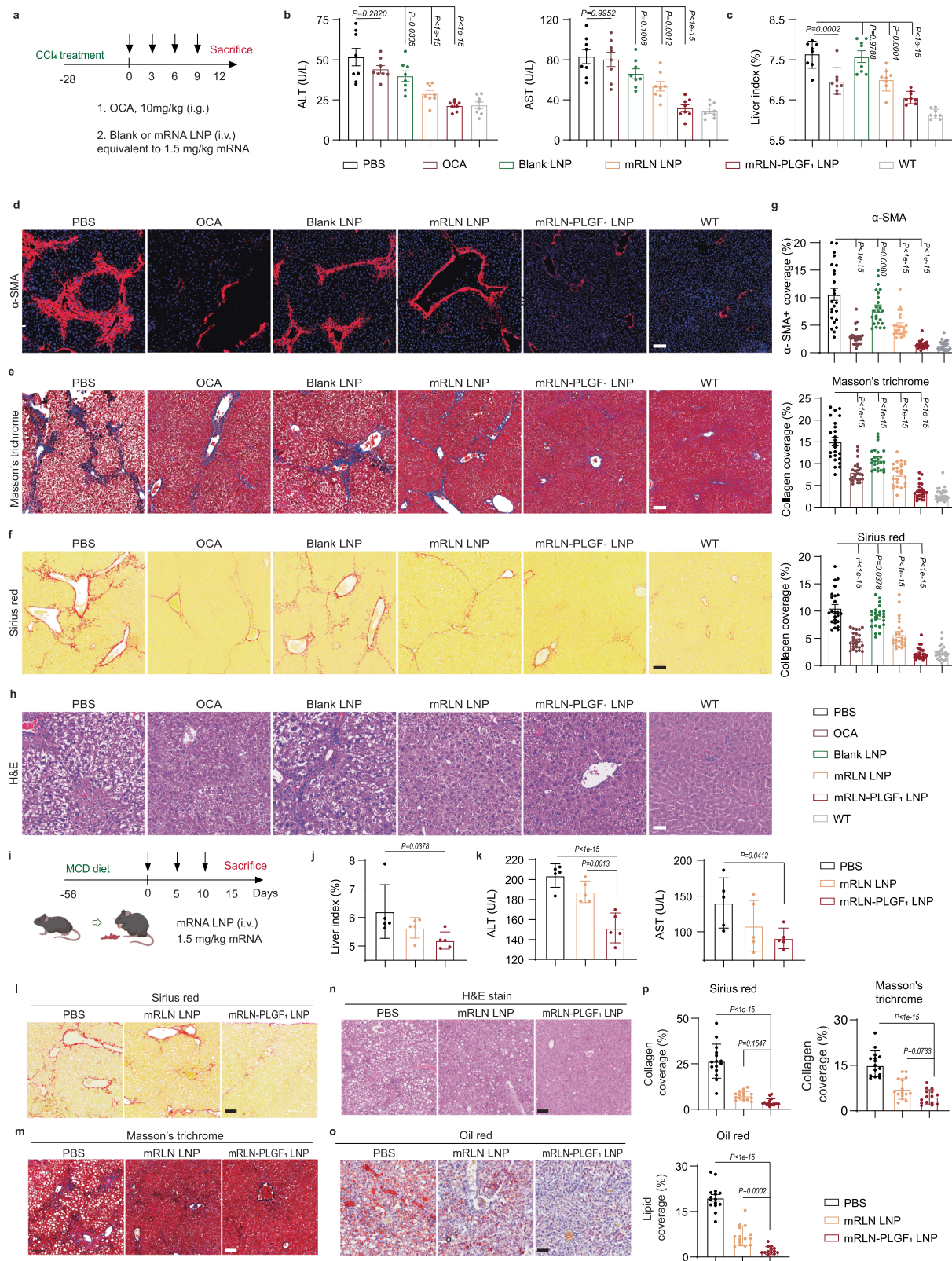
To demonstrate the versatility of the FORT strategy, we selected IL-10 as another therapeutic protein known for its anti-inflammatory effects (Supplementary Fig. 32). By incorporating the PLGF peptide at the C-terminus of IL-10, we enhanced its interaction with ECM proteins (Supplementary Fig. 25). Compared with the unmodified mIL10 LNP, we observed that mIL10-PLGF₁ LNP exhibited a stronger antifibrotic effect within the liver (Supplementary Fig. 32b–i). Parameters such as liver index, ALT/AST levels, and the area of liver fibrosis were significantly reduced after treatment with mIL10-PLGF₁ LNP. Moreover, mIL10-PLGF₁ LNP exhibited a notable reduction in inflammatory cytokine levels. These findings highlight the broad applicability of FORT strategy for delivering other soluble therapeutic proteins for fibrosis treatment.

The anti-fibrosis effect of the FORT strategy using therapeutic RLN was further examined in mice fed on an Methionine-choline-deficient (MCD) diet. The model is accompanied by fat accumulation and liver fibrosis. We extended the dosing intervals to five days to challenge the retention capacity of the strategy (Fig. 6i). Consistently, mRLN-PLGF₁ demonstrated enhanced therapeutic effects compared to the unmodified mRLN LNP (Fig. 6j–p). In fact, the reduction in collagen coverage in the liver was twofold greater in the mRLN-PLGF₁ group than in mRLN group, as evidenced by Sirius red and Masson's trichrome staining (Fig. 6l, m). In the mRLN-PLGF₁ group, significantly lower levels of liver index, AST/ALT levels were observed (Fig. 6j, k). Interestingly, Oil red O staining revealed that mRLN-PLGF₁ LNPs effectively cleared lipid droplets in the MCD-induced mouse model. We conducted gene expression analysis in treated mice to identify mechanisms involved in this change. Our results showed a more pronounced reduction (~2–10-fold) in inflammatory cytokines (e.g., $Il-1\beta$, $Il-6$) productions in mice treated

with mRLN-PLGF₁ LNPs group compared to mRLN LNPs (Supplementary Fig. 33). Additionally, there was a slight decrease in expression of fatty acid uptake genes (*Fabp1*, *Cd36*, *Lipin1*) and lipogenesis genes (*Srebp1c*, *Fasn*, *Dgat2*), along with upregulation of genes involved in lipid oxidation (*Acot1*). These findings suggest that ATRA LNPs formulated mRLN-PLGF₁ have the potential to remodel the MASH microenvironment by affecting both fibrotic and lipid biosynthesis pathways.

Low-dose combination of mRLN-PLGF₁ and mIL-10-PLGF₁ LNP leads to outstanding performance in hamster models with MASH

To further investigate the potential of FORT strategy in clinical application, we applied it to a more clinically relevant MASH model using hamsters fed with CDHFD diet. This model closely mimics the metabolic profile and pathogenesis of humans (Fig. 7a, Supplementary Fig. 2). Both mRLN-PLGF₁ and mIL-10-PLGF₁ were formulated with ATRA LNPs and administered through jugular vein (Fig. 7b). We extended the therapeutic intervals to 6 d per dose. Significant echo signal reduction was observed using ultrasound imaging within 18 days when treated with either mono or combined therapy (Fig. 7c and Supplementary Fig. 34). Remarkably, the combination of mRLN-PLGF₁ and mIL-10-PLGF₁ LNP substantially ameliorated liver fibrosis and inflammation (Fig. 7c–k). This was characterized by the reduced and more homogenous echo intensity, as well as the lower levels of ALT/AST (Fig. 7e) and total cholesterol/triacylglycerol (TC/TG) compared to the sham group (Fig. 7d, k). Interestingly, mIL-10-PLGF₁ LNPs significantly reduced TC/TG levels in the circulation, while mRLN-PLGF₁ was more effective in downregulating liver fat and fibrosis, suggesting a potential synergism between the two regimens. After combo therapy, collagen disposition in liver was similar to the WT group (Fig. 7f, g). Combo therapy almost eliminated the accumulation of lipid droplets (Fig. 7h, i). We further investigated the genes associated with fibrosis and lipid metabolism. mRLN-PLGF₁ LNP monotherapy induced a more substantial reduction of pro-fibrogenic factors, while the combo therapy fell in between, with ~5.7-fold, ~12.8-fold, ~8.0-fold downregulation of $TGF-\beta$, α -SMA, $COL1\alpha1$, along with significant upregulation of $MMPs$, when compared to the sham group (Fig. 7l). Both mRLN-PLGF₁ and mIL-10 showed slight inhibition of lipogenesis genes (*SCD1*, *SREBP1C*), consistent with those observed in the MCD models (Fig. 7l). Notably, promotion of fatty acid β -oxidation was observed in both therapies (Fig. 7l). These results demonstrate the feasibility of applying multiple FORT proteins to achieve synergistic effects and facilitate recovering of MASH. Moreover, neither of the proposed mRNA therapies induced histological abnormalities in major organs or caused significant changes in body weight when compared with sham treatment, suggesting negligible systemic toxicity, low immunogenicity or immunosuppression (Supplementary Fig. 35).



Acute and long-term preclinical toxicity study of FORT

Ensuring the biosafety of drug candidates is crucial for their clinical translation. We intravenously injected mRLN-PLGF₁-LNPs into healthy Institute of Cancer Research (ICR) mice, gradually increasing the doses from 0.75 to 5 mg/kg, with a total of three doses administered. As depicted in Supplementary Fig. 36, no significant changes were

observed in any of the tested blood biochemistry parameters following single or multiple doses up to 3 mg/kg. Moreover, no evident tissue damage was detected in the major organs, indicating that mRLN-PLGF₁-LNPs exhibited relative safety within the 3 mg/kg dose range in mouse models. However, a slight increase in ALT or Blood urea nitrogen levels was observed after acute dosing of 5 mg/kg or multiple

Fig. 6 | Anti-fibrosis effects of mRLN-PLGF₁ LNP in CCl₄-induced fibrotic or methionine/choline deficient (MCD) diet induced MASH models. **a** Schematic representations of the CCl₄-induced liver fibrosis models and treatment schedules for ATRA LNP formulated mRLN or mRLN-CBDs (1.5 mg/kg mRNA). **b** Serum alanine transaminase (ALT) and aspartate transaminase (AST) from CCl₄-induced fibrotic mice with all treatment groups after 4 doses treatment ($n = 8$ mice). **c** Liver index (liver weight/body weight%) of all treatment groups from CCl₄-induced liver fibrotic mice model ($n = 8$ mice). Representative IF staining of α -SMA (**d**), Masson's trichrome (**e**), Sirius red (**f**), scale bar represents 250 μ m. **g** Quantification of (**d–f**). The quantification was performed in three randomly selected fields per mouse (from $n = 8$ mice per group). **h** Hematoxylin-eosin (H&E) staining in CCl₄-induced liver fibrotic mice with all treatment groups after treatment ($n = 8$ mice), scale bar represents 100 μ m. **i** Schematic representations of the MCD diet induced MASH

mouse model and treatment timeline for ATRA LNP formulated mRLN and mRLN-PLGF₁ (1.5 mg/kg mRNA). **j** Liver index (liver weight/body weight %) of all treatment groups from MCD diet induced MASH models ($n = 5$ mice). **k** Serum ALT and AST of all treatment groups from MCD mice ($n = 5$ mice). Representative histochemical staining of Sirius red (**l**), Masson's trichrome (**m**), H&E (**n**) and Oil Red O (**o**) in MCD mice with all treatment groups ($n = 5$ mice), scale bar represents 250 μ m in (**l, m**), 100 μ m in (**n**). **p** Quantification of the coverage% area of collagen in (**l**) and (**m**) and lipid accumulation area in (**o**). The quantification was performed in three randomly selected fields per mouse ($n = 5$ mice). Data were presented as mean \pm SD, “n” indicates biologically independent samples. Statistical significance was calculated through One-way ANOVA with Dunnett test. Figure 6a and i were created with BioRender.com released under CC BY-NC-ND 4.0. Source data are provided as a “Source Data” file.

doses, indicating some impacts on the liver and kidney. Nevertheless, no significant organ damage was observed at this dose. Overall, our findings confirm the favorable safety profile of the FORT strategy, encompassing both the vehicle, mRNA and the encoded proteins, in preclinical rodent models, thereby suggesting the potential for clinical translation. However, further safety assessments in non-rodent models are necessary to obtain a comprehensive safety profile prior to advancing to clinical trials.

Discussion

Fibrotic diseases are a leading cause of morbidity and mortality worldwide. Here we present a new approach to treating fibrotic diseases, termed “Fibrosis overexpression and retention (FORT)”. In this two-part strategy, we design (1) retinoic acid LNPs which distributed retinoids on the surface of the particles, facilitating RBP-4 mediated endocytosis and sprouting/fusion-mediated endosome escape in HSCs, and (2) modified mRNAs which encode for CBDs allowing us to anchor expressed therapeutic fusion proteins to fibrotic ECM. We believe this is the first time that fibrotic lesions have been targeted and treated in this way. This approach offers advantages over current modalities as it confines the therapeutic protein to the disease region, extending the duration of action and minimizing systemic exposure.

Fibrotic liver diseases such as MASH and cirrhosis are characterized by capillary base thickening and ECM accumulation. These biophysical changes increase difficulty for therapeutic delivery. In our study, we found commercial LNP formulations were ~10-fold less effective at delivering mRNA to MASH animal models. We proposed the physical incorporation of Food and Drug Administration (FDA)-approved molecules to enhance mRNA delivery to HSCs in fibrotic livers. Retinoid derivatives were chosen due to their high no-observed-adverse-effect level (NOAEL) in patients and their established suitability for targeting HSCs. Although targeted moieties such as antibodies, nanobodies, and aptamers have been widely explored to improve HSC targeting, they often present challenges in terms of scaling up complexity and batch-to batch variability⁴³. In contrast, the physical incorporation⁴⁴ of hydrophobic moieties into lipid bilayers presents a simple targeting approach with ease of manufacturing. This approach also facilitates incorporation of small molecules over a wide dose range.

Our study focused on exploring the structure-activity relationship of the retinoid derivatives by physically encapsulating various moieties within LNPs. Surprisingly, conventional retinol or uncharged esters did not exhibit effective targeting to HSCs, while carboxylic acid derivatives demonstrated improved targeting. Mechanistic studies suggested that these derivatives may induce a spatial reorganization of lipids when condensed with mRNA, affecting RBP-4-mediated cell uptake. Additionally, we discovered that the endosomal membrane of HSCs is more rigid than that of hepatocytes. ATRA LNPs with enhanced sprouting and fusion rate demonstrated superior fusion with HSC-endosome mimicking membranes, potentially promoting RNA release.

To enhance therapeutic efficacy, new strategies enabling protein retention without compromising biological activity are required. Previous studies have demonstrated that binding therapeutic antibodies or proteins to collagen can enhance local accumulation. However, the applications have been limited by delivery challenges. In our study, we delivered designed mRNA encoding for therapeutic proteins fused to CBD to facilitate retention in the MASH fibrotic lesion. We selected a CBD motif from endogenous protein domains, as opposed to peptide sequences obtained from display techniques, since the endogenous CBDs offer advantages such as lower immunogenicity and higher specificity. Notably, we found that the addition of multiple CBDs does not further enhance binding or efficacy. In contrast, it might induce mis-folding, compromising therapeutic efficacy. Therefore, we chose to combine therapeutic proteins with a single CBD, identified from PLGF.

RLN is a promising therapeutic protein for treatment of fibrosis currently in clinical trials⁴⁵. However, clinical failures of RLN peptides have been primarily attributed to undesirable pharmacokinetics⁴⁶. Additionally, RLN lacks an intrinsic CBD to facilitate its interaction with the ECM. We demonstrated that our modified RLN-PLGF₁ protein improved fibrotic liver accumulation of RLN protein and increased anti-fibrosis activity in three MASH models. We also extended the use of FORT strategy to other secretable proteins such as IL-10.

In conclusion, we have developed a new type of mRNA LNP therapy for the treatment of fibrosis, termed FORT. By incorporating an FDA-approved retinoic acid in LNPs, the expression of RNA therapeutics in fibrotic liver was significantly improved. Further, the addition of an endogenous CBD domain from PLGF to mRNA sequences generates a fusion protein with improved retention in fibrotic lesions. Delivery of therapeutic proteins using these strategies ameliorates fibrosis in animal models. We believe this approach can be broadly applied to other chronic inflammatory diseases that are not amenable to direct injection but can be targeted using LNPs.

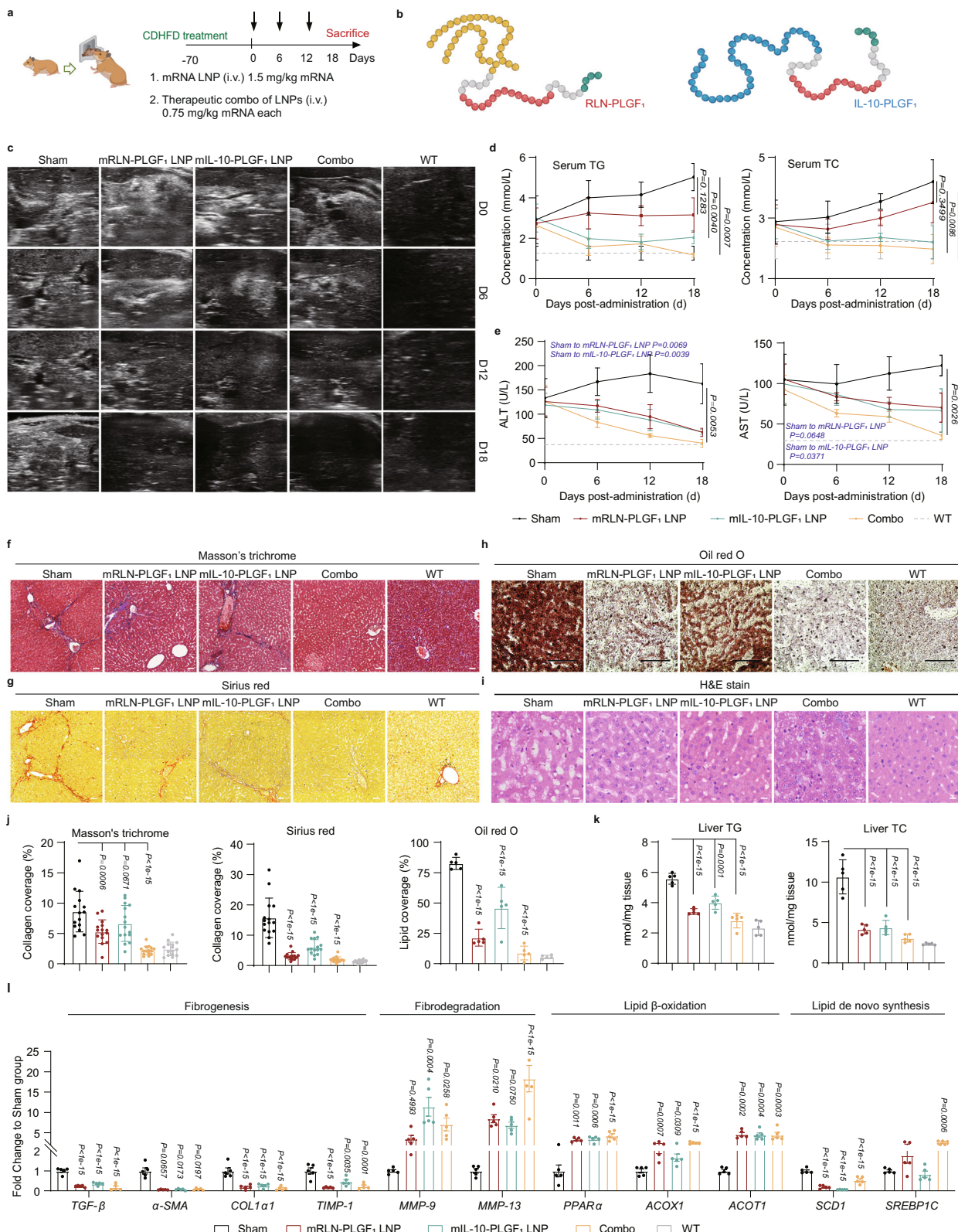
Methods

Ethical statement

Our research complies with all relevant ethical regulations. All animal research was in compliance with ethical regulations approved by Peking University's Institutional Animal Care and Use Committee.

Materials

All the ionizable lipids containing DLin-MC3-DMA (MC3), 6-((2-hexyldecanoxy)oxy)-N-(6-((2-hexyldecanoxy)oxy)hexyl)-N-(4-hydroxybutyl)hexan-1-aminium (ALC-0315) and 1-octylnonyl 8-(2-hydroxyethyl)6-O-0-(undecyloxy)hexyl amino-octanoate (SM-102) were purchased from Avanti Polar Lipids, Inc. Helper lipids containing cholesterol, 1,2-Dioctadecanoyl-sn-glycero-3-phosphocholine (DSPC) and 1,2-dimyristoyl-rac-glycero-3-methoxypolyethylene glycol-2000 (DMG-PEG2000) were bought from A.V.T. Pharmaceutical Tech Co., Ltd. Small-molecular retinoids containing retinol, 4-keto-retinol, all-trans-retinoic acid (ATRA), 13-cis retinoic acid (13-CRA), Acitretin (A-



VA), were purchased from Sigma-Aldrich, 9-cis retinoic acid (9-CRA), fenretinide and acetyl-retinol were purchased from Macklin Co., Ltd, bexarotene and tamibarotene were obtained from MedChemExpress Co., Ltd. Firefly luciferase mRNA (mLuc) was provided by Proxbybio. Collagen I, II was purchased from Sino Biological and Collagen IV from Sigma. Human and mouse RBP-4 were purchased from Sino Biological Inc. Purified RLN, RLN-PLGF₁, RLN-Fc, and cell lysates containing RLN and RLN-PLGF₁ were provided by KeyMed Biosciences. The small-

molecular uptake inhibitors and carbon tetrachloride were purchased from Macklin Co., Ltd. MCD diet and choline-deficient high-fat diet (CDHFD, 45% kcal) was purchased from Dyes Inc. All the plasmid sequences were provided by Genscript Co., Ltd. Primers and siRNA were from Tsingke Biotechnology Co., Ltd. All cell lines and fetal bovine serum (FBS) were purchase from Procell Life Science & Technology Co., Ltd. Other reagents for basal culture were bought from Meilunbio Co., Ltd. ELISA kits for mouse IL-6, TNF- α , IL-1 β and IFN- γ

Fig. 7 | Low-dose combination of mRLN-PLGF₁ and mIL-10-PLGF₁ delivered by ATRA LNPs for treating hamsters with MASH. **a** Schematic representations of the CDHFD induced MASH hamster models and the treatment schedules for single and combinatorial administrations of ATRA LNP formulated mRLN-PLGF₁ and mIL-10-PLGF₁ through jugular vein. Hamsters on CDHFD with sham surgery in the jugular vein were served as a control. **b** The schematic structures of RLN-PLGF₁ and IL-10-PLGF₁ recombinant proteins. **c** Representative in vivo ultrasound imaging of livers from the CDHFD-induced MASH hamsters from all treatment groups at 0, 6, 12 and 18 d post the first dose treatment. Higher intensity and heterogeneity of the hepatic echogenicity reflected the more aggressive fibrosis conditions. Serum total cholesterol/triacylglycerol (TG and TC) in **d**, serum ALT and AST in **e** from CDHFD induced MASH hamsters in all treatment groups at 0, 6, 12, 18 d post the first dose treatment ($n = 5$ hamsters). Representative histochemical stains for all the

treatment groups from CDHFD-induced MASH hamsters, including Masson's trichrome (**f**), Sirius red (**g**), Oil Red O (**h**) and H&E (**i**) staining ($n = 5$ hamsters), scale bar represents 250 μ m in (**f**, **g**), 100 μ m in (**h**, **i**); **j** Quantification of the coverage% area of collagen in (**f**, **g**) and fat accumulation area in (**h**). The quantification was performed in three randomly selected fields per hamster in (**f**, **g** and **i**), one randomly selected field in (**h**). ($n = 5$ hamsters per group, $n = 3$ fields per hamster); **k** TG and TC level in liver after treatment ($n = 5$ hamsters); **l** Relative mRNA expression of biomarkers for fibrogenesis, fibrodegradation, lipid- β -oxidation and lipid de novo synthesis in liver of CDHFD induced MASH hamsters with all treatment groups after treatment ($n = 5$ hamsters). Data were presented as mean \pm SD, "n" indicates biologically independent samples. Statistical significance was calculated through One-way ANOVA with Dunnett test. Figure 7a and b were created with BioRender.com released under CC BY-NC-ND 4.0. Source data are provided as a "Source Data" file.

were purchased from Solarbio Science & Technology Co., Ltd, mouse RLN-1 from Boster Bio and cAMP from Elabscience Biotechnology Co., Ltd. The qPCR primers and siRNA sequences were listed in Supplementary Table 8. All antibodies used in this study were listed in Supplementary Table 9.

The source of cell lines: LX-2 cell (CL-0560, Procell); NIH/3T3 cell (CL-0171, Procell); THP-1 cell (CL-0233, Procell); RAW264.7 cell (CL-0190, Procell); 293F cell (R79007, ThermoFisher).

mRNA synthesis

mRLN, mRLN-PLGF₁, mRLN-Fc, mIL-10-PLGF₁, mLuc and mCre were synthesized using T7 polymerase mediated in vitro transcription (IVT) system from linearized pUC57 plasmid vectors containing T7 promoter, 5' and 3' untranslated regions (UTRs) and a poly A tail (100 nt). The clean-cap AG 5' capping (Cap 1) and 1-methylpsuedo-uridine UTP were added to the transcription reaction. The uridine-5' triphosphate (UTP) was fully replaced with 1-methylpsuedo-uridine UTP to improve protein translation and minimize immunogenicity generated from synthesized mRNA. IVT reactions were conducted according to the manufacturers' protocols (Hongene Biotech Inc., China). The mRNAs encoding fusion proteins containing 11 different CBD domains (i.e., RLN and IL-10) for initial screening were synthesized from linearized pUC57 plasmid vectors with the absence of poly A sequence. Poly A were added after IVT reactions using Poly A Polymerase Tailing Kit (Beyotime Biotechnology). The CDS sequences of mRNAs used in the current study were listed in Supplementary Data files 4. Purity of the linearized plasmids and synthesized mRNAs were validated by gel electrophoresis (ChemiScope Capture) (Supplementary Figs. 23 and 26).

Lipid nanoparticle preparation and characterization

LNPs were prepared either by hand mixing or microfluidic mixing as previously described. Briefly, an aqueous solution of the mRNA and an ethanolic solution of the lipid components were mixed at a ratio of 3:1, respectively. The ethanol phase consists of ionizable ALC-0315 (Avanti), 1, 2-distearoyl-sn-glycero-3-phosphocholine (DSPC, AVT, China), cholesterol (AVT, China) and 1,2-dimyristoyl-sn-glycerol, methoxypolyethylene glycol (DMG-PEG2000, AVT, China), a series of FDA approved retinoids at the predetermined molar ratio (Supplementary Table 1). The aqueous phase was prepared in 10 mM citrate buffer containing 0.14 μ g/ μ L mRNA. After mixing, the obtained LNPs were dialyzed against 1 \times PBS in dialysis bag at 4 °C overnight.

mRNA concentration and encapsulation efficiency of LNP were measured using Quant-it RiboGreen RNA assay (Invitrogen). The hydrodynamic diameter and zeta potential were measured by dynamic light scattering (Zetasizer software version 7.12, Zetasizer Nano ZSP, Malvern). The morphology of LNPs was characterized by transmission electron microscopy (TEM) and cryo-electron microscopy (cryo-EM). TEM image was acquired using JEM-1400 Flash Electron Microscope in RADIUS 2.1 software. For cryo-EM, the prepared LNP were dialyzed in

20 mM Tris (pH 7.4) containing 8% sucrose 4 °C overnight and then concentrated to 0.5 mg/ml total RNA by ultrafiltration. Cryo-EM image was acquired using Themis 300 in Velox 3.8 software (Thermo Fisher Scientific).

Small angle neutron scattering (SANS)

In this work, SANS was performed on the Small Angle Neutron Scattering (SANS) instrument at China Spallation Neutron Source²⁹. The incident neutrons with wavelength of 1–10 Å were defined by a double-disc bandwidth chopper, which is collimated to the sample by a pair of apertures. The experiment used the sample to detector distance of 4 m and a sample aperture of 6 mm. The 1 m square detector array composed of 120 linear He-3 gas tubes with the diameter of 8 mm, which covers the Q-range between 0.01 Å⁻¹ and 1 Å⁻¹. The presented data corresponds to ~120 min of data collection time for each sample (@140 kW). For all SANS data, background signals from the solvent, sample cell, and the instrument were subtracted by separate runs to measure their scattering contributions. Neutron data were normalized and corrected for transmission and detector efficiency and set to absolute units. Modeling and simulation details are provided as below:

Samples prepared for the SANS experiment had the protonated ATRA (SLD (scattering length density, ρ) 0.798×10^{-6} Å⁻²) replaced with the ATRA-d5 (SLD 1.81×10^{-6} Å⁻²), so that its location is highlighted in the LNP (average SLD 0.25×10^{-6} Å⁻²), while the overall structure of the LNP remains unperturbed. A set of samples with all-trans-retinoic acid containing lipid nanoparticles (ATRA LNPs) (ALC-0315/DSPC/Cholesterol/DMG-PEG₂₀₀₀/ATRA = 50:10:28.9:1.5:9.6 (mol), 0.3 mg/mL mRNA, ~5 mg/mL total lipid) was prepared with solvent at four different H₂O/D₂O ratios for contrast variation measurement.

Following earlier SANS studies on the LNP system, an integrated core-shell sphere (assuming polydispersed core radius) + Gaussian peak model was chosen to fit the data^{16,47,48}. The distribution of all components in LNP as well as their relationship to the key fitting parameters have been listed in Supplementary Table 3. All the listed fitting parameters, except for the ρ_{water} , were set as fitting parameters constrained to be unique for the whole sample sets with varying H₂O/D₂O ratio. Additionally, as the scattering length density and the ratio of the various LNP components are known parameters, the average LNP (dry) SLD are calculated accordingly and was used as another constrain condition during the fitting:

$$\rho_{\text{LNPdry}} = \rho_{\text{drycore}} \varphi_{\text{drycore}} + \rho_{\text{shell}} \varphi_{\text{shell}}$$

φ_{drycore} and φ_{shell} correspond to the volume fraction of the drycore and shell in the LNP with the volume contribution from water excluded. The simultaneous data fitting was performed using SasView.

Based on the fitted results of the SLDs and volumes of the core and shell phases (Supplementary Table 4), the partitioning of ALC-0315, cholesterol and ATRA-d5 in the core and shell phases were

thus estimated using the equations given below:

$$V_{\text{drycore}} = (\varphi_{\text{mRNA}} + \varphi_{\text{ALC}} f_{\text{ALC}} + \varphi_{\text{cholesterol}} f_{\text{cholesterol}} + \varphi_{\text{ATRA}} f_{\text{ATRA}}) * (V_{\text{drycore}} + V_{\text{shell}})$$

$$\rho_{\text{drycore}} = (\varphi_{\text{mRNA}} \rho_{\text{mRNA}} + \varphi_{\text{ALC}} f_{\text{ALC}} \rho_{\text{ALC}} + \varphi_{\text{cholesterol}} f_{\text{cholesterol}} \rho_{\text{cholesterol}} + \varphi_{\text{ATRA}} f_{\text{ATRA}} \rho_{\text{ATRA}}) * \frac{(V_{\text{drycore}} + V_{\text{shell}})}{V_{\text{drycore}}}$$

The symbol φ here refers to the volume fraction of each component relative to the overall dry LNP volume and f refers to the fraction of the corresponding component partitioned in the core phase. As it is impossible to obtain the exact values for the three “ f ’s with only two equations, only the possible ranges of the volume distribution of these three components were given (Supplementary Table 5).

Cells culture and assays

Cell lines were maintained in DMEM or RPMI-1640 medium supplemented with 10% fetal bovine serum (FBS, Procell, China) and penicillin, streptomycin (Meilunbio, China). For activation of 3T3 cells, TGF-β1 was added at 10 ng/ml for 24 h.

In vitro transfection

Cells were plated in white, clear-bottom 96-well plates at 4000 cells per well for LX-2 cells and 1×10^4 cells per well for primary hepatocytes. On the second day, mLuc LNP was added to cells at 0.1 μg mRNA per well. After 24 h incubation, the transfection efficiency was measured by Firefly-Glo Luciferase Reporter Assay Kit (Yeasen Biotechnology Co., Ltd) following the manufacturer’s protocol, using BioTek synergy H1 microplate reader.

In vitro cell uptake

Primary hepatocytes and LX-2, a HSCs were plated in 96-well plates at a density of $\sim 10^4$ cells per well 24 h prior to the experiment. The cells were pre-incubated with small-molecule endocytic inhibitors for 15 min. Small molecule endocytic inhibitors used in current study are listed below: cytochalasin D used for F-actin polymerization inhibition at 2.5 μg/mL; methyl-β-cyclodextrin used for cholesterol/caveolae depletion at 2.5 mg/mL; nocodazole used for microtubule inhibition at 5 μg/mL; poly I used at the scavenger receptor inhibitor at 10 μg/mL; wortmannin used for inhibiting phosphoinositide pathway at 100 ng/mL and dynasore used for GTPase dynamin inhibition at 10 μg/mL. In addition, siRNA used for the knockdown of gene of STRA6, the RBP-receptor, was added at 200 nM 24 h at 37 °C prior to LNP incubation. After pre-incubation with small molecules and siRNA, the supernatant was aspirated, washed twice with PBS. Then, 2.5 mol% BODIPY-lipid labeled LNPs (equivalent to 0.2 μg RNA per well) were added into each well of cells. After 2 h incubation at 37 °C, the wells were washed 3 times with cold PBS and replaced with fresh media. The cellular uptake was determined by CellPathfinder, the high content imaging and analysis system (Cell Voyager CV8000, Yokogawa). Nucleus and lysosome were stained with Hoechst 33342 (1 μg/mL) and LysoTracker Red DND-99 (10,000× dilute) at 10 min before imaging. Flow cytometric analysis was performed 24 h after LNPs treatment (CytExpert software, CytoFLEX, Beckman). The mean fluorescence intensity was applied for quantification (Flowjo V10).

Live-cell imaging of mRNA release

Intracellular release of mRNA from LNPs was visualized using an inverted Zeiss LSM880 confocal microscope. Airyscan array detector unit (Carl Zeiss AG) was used to strengthen and visualize the cytosol mRNA signals within the live cells. Five % BODIPY-lipid and 100% Cy-3-UTP replaced mRNA were applied for tracing the intracellular behavior of LNP and mRNA. Cells were treated with the labeled LNP with mRNA

at a concentration of 2 μg/mL and incubated for 2 h at 37 °C. Subsequently, the media were replaced with fresh media containing 1 μg/mL Hoechst 33342, and endosome release was observed using a 100× Plan-Neofluar 1.3 numerical aperture (NA) oil-immersion objective. For all experiments, the field of view (FOV) was set to 354, 25 μm × 354, 25 μm (full). The pinhole was set to 1 Airy Unit for all channels. The acquired imaging data were processed using Zen2.3 software (blue edition) for analysis.

Microscale thermophoresis (MST) assay

The binding affinities between RBP-4 to free retinoids, empty, and mRNA-loaded LNP were measured using a NanoTemper Monolith NT.115 instrument in MO. Control software (NanoTemper Technologies, Munich, Germany). Firstly, RBP-4 was adjusted to a concentration of 10 μM and labeled with MonolithTM NT.115 protein Labeling Kit RED-NHS (Nanotemper Technologies, Germany), following the manufacturer’s protocols. The labeled RBP-4 was then purified by gel filtration and diluted to a 250 nM solution using PBS containing 0.05% Tween 20 (PBS-T), ensuring that the fluorescent intensity of RBP-4 during the MST assay was ~500 response units (RU). LNPs with an initial concentration of 1 mg/mL (total lipid) were serially diluted (16-point, 1:1 dilution in PBS-T) and mixed in equal volume with the pre-diluted RBP-4. The mixture was incubated for 1 h at room temperature. After incubation, the samples were loaded into premium treated capillaries and measured using the NanoTemper Monolith NT.115 instrument. The dissociation equilibrium constant (KD) values were fitted according to the KD Model (1:1 binding mode), by the NanoTemper Monolith affinity software MO. Affinity Analysis v2.3 (NanoTemper Technologies, Germany).

The binding affinity measurement between the RLN fusion protein (with or without the presence of collagen) and surface receptor RXFP1 was carried out using crude cell lysates. In detail, plasmids encoding RLN-His6 or RLN-PLGF1-His6 were transfected into 293F cell line. After proliferation, cells were diluted to $\sim 10^8$ cells/mL and lysed. To label and calculate the concentration of the His6 tag-labeled protein in the supernatant, cell debris was removed, and a 16-point 1:1 serial dilution was performed. The diluted aliquots were then incubated with RED-tris-NTA dye at a final concentration of 25 nM for 30 minutes. Subsequently, all samples were loaded on the NanoTemper Monolith NT.115 instrument. A binding curve was generated between the Red-tris-NTA dye and the cell lysates containing His-tag labeled proteins. Concentration of the His-tag labeled protein was calculated from the tipping point of the simulated binding curve. Accordingly, equimolarly labeled lysates were then incubated with serially diluted collagen IV to assess the lysate-to-collagen binding affinity.

To evaluate the interaction of RLN or RLN-PLGF1 with the receptor RXFP1 on RXFP1+ cells in the presence or absence of collagen, 1 μM collagen IV (concentration at the saturation plateau of the binding curve) was added to the cell lysates. The binding affinity between the lysates and RXFP1 was further determined by incubating the labeled lysates with serially diluted RXFP1+ and RXFP1- 3T3 cells. The same instrument and analytical software as described in Method 4 were used for this analysis, results were presented in Supplementary Fig. 30.

Surface plasmon resonance

The SPR binding assays were performed using Biacore 8K⁺ (Biacore, Cytiva). Recombinant collagen II (Sino Biological) was immobilized onto a CM5 sensor chip using standard amine coupling at 25 °C. The reference flow cell was activated and subsequently blocked with BSA. The immobilization levels of collagen II were consistently around 3000 RU. To evaluate the binding affinity, various concentrations of RLN, RLN-PLGF1, RLN-Fc (6.25, 12.5, 25, 50, 100, and 200 μM) were injected into the channel. The binding assays involved subtracting the response observed in the reference flow cell containing BSA to account for non-

specific binding. Regeneration of the sensor chip was achieved by performing extended washes with NaOH (5 mM) after each sample injection. The dissociation constants (KD) were determined by fitting the obtained data sets to a steady-state affinity model using the Biacore 8K Evaluation Software.

In vitro collagen binding assay

Cells were seeded in 6-well plates at a density of -5×10^5 cells overnight and treated with mRNA-LNP. After 24 h of incubation, the cell culture supernatant was collected and incubated in 96-well ELISA plates that were pre-coated with collagen I, collagen II, collagen IV, and BSA (10 µg/mL). The plates were then blocked with a solution of 2% BSA in PBS-T. Following a 1 h incubation at 37°C, the supernatant was removed, and the plates were washed and incubated with rabbit anti-Flag-tag antibody for 1 h at 37°C. After incubation, the plates were washed and incubated with HRP-conjugated goat anti-rabbit antibody for additional 1 h at room temperature. The collagen binding capacity was determined by measuring the absorbance of colorimetric TMB substrate, which reacts with HRP at 450 nm (Biotek Synergy HI, Gen5 3.11 software).

Molecular modeling and dynamics simulation of fusion proteins

To predict the molecular models of all fusion proteins, we employed ColabFold V1.5.2³⁰ and run it in Google Colaboratory. We used the crystal structure (PDB: 6RLX) of human RLN-2 peptide³¹ as a template to predict the RLN-PLGF₁ fusion protein. Among the generated models, the one with the highest pLDDT score (predicted local distance difference test) was selected as the best model for further modeling and molecular dynamics experiments. For predicting RLN-PLGF₃ and RLN-Fc, the previously predicted RLN-PLGF₁ model and the crystal structure of human RLN-2 peptide (PDB:6RLX) were used as templates. Again, the models with the highest pLDDT score were selected as the best models for the subsequent molecular dynamic experiments.

To carry out the molecular dynamics simulations, Groningen Machine for Chemical Simulations v2019.5 (GROMACS) was employed. The simulation runs lasted for 100 ns for RLN-PLGF₁ and 200 ns for RLN-PLGF₃ and RLN-Fc. The CHARMM27 all-atom force field³² was used for these simulations. Each system was placed in a cubic water box consisting of the TIP3P water model, which was neutralized with counter ions. The system was initially minimized using the steepest descent algorithm through 1000 steps to eliminate any unfavorable contacts. Subsequently, the equilibration processes were conducted using constant number, volume (NVT), and temperature (NPT). The protein backbone was constrained, while the solvent molecules and counter ions were allowed to move freely. The NVT was carried out for 100 ps at 300 K. The NPT was executed for 100 ps at 1 bar. The restraints on heavy atom bonds were imposed using the LINCS algorithm³³. The Particle Mesh Ewald³⁴ method was used to calculate long-range electrostatic interactions, with a cutoff value of 10 Å for short-range interactions. Periodic boundary conditions were implemented to avoid edge effects. The coordinate data were saved with a time step of 2 fs for every 1 ps. Finally, Visual Molecular Dynamics³⁵ and Pymol³⁶ were used for the evaluation of the results.

Animal models

All animal research was approved by the ethical regulations of Peking University's Institutional Animal Care and Use Committee. The living environment of animals were maintained at -25 °C and 40% humidity with a 12 h light/dark cycle, with free access to standard food and water unless otherwise stated. Male animals were selected for our experiments according to previous literature and relevancy to clinical conditions⁴⁹. For models of CCl₄-induced liver fibrosis, 8-week-old male C57BL/6J mice were intraperitoneal injected with CCl₄/olive oil (7/13, v/v, 50 µL per mouse) three times a week for a total of 4 or 6 weeks. For MASH models of C57BL/6J mice and Syrian golden

hamster, 8-week-old male animals were fed with MCD diet (catalogue number 59580, Dyets) for 8 weeks or CDHFD (catalogue number: HF45, fat diet with 45 kcal% Diets) for 10 weeks. Fibrosis or MASH level were monitored by measuring serum AST and ALT levels. Other wild-type mice and hamsters were fed on chow diet (catalogue number: HD8015, Huanyu Bio). For all the animals, euthanasia was performed at the pre-determined timepoints or post-study via carbon dioxide asphyxiation followed by cervical dislocation in accordance with American Veterinary Medical Association (AVMA) guidelines.

In vivo expression

mLuc LNPs were i.v. administrated to healthy mice or mice with liver fibrosis (8-week-old male C57BL/6J mice with another 4–6 weeks CCl₄/olive oil treatment for liver fibrosis model, the same week-old mice were as healthy control, 0.25 mg mLuc/kg). At 2, 6, 12, and 24 h after injection, bioluminescence imaging was performed using IVIS imaging system in Living Image 4.3.1 software (Perkin Elmer). Hamsters with MASH (8-week-old male hamsters with another 10 weeks CDHFD diets, the same week-old hamsters were as WT control) were anesthetized by inhalation of isoflurane. A midline incision was made between the chin and sternum. LNPs at a dose of 0.25 mg/kg were injected through the jugular vein after blunt separation of the peripheral muscle⁵⁰⁻⁵². Bioluminescence images were taken following the same process as described above. Animals were euthanized by CO₂ inhalation for ex vivo expression.

In vivo distribution

The in vivo distribution of ALC-0315 and ATRA LNPs were evaluated in CCl₄-induced liver fibrosis mice (8-week-old male C57BL/6J mice with another 4 weeks CCl₄/olive oil treatment). The mice were i.v. treated with DiR-labeled ALC-0315 and ATRA LNPs (0.25 mg/kg). At 6 h after injection, the fluorescence images of heart, liver spleen, lung and kidney are observed by IVIS imaging system in Living Image 4.3.1 software (Perkin Elmer). Moreover, the liver tissues were fixed, dehydrated, frozen, and loaded on the glass slide for immunofluorescence staining.

mRNA delivery and expression in the tdTomato mice

To evaluate mRNA expression in different cell types, CCl₄-induced liver fibrotic LoxP-flanked tdTomato reporter mice with C57BL6/J background were utilized (8-week-old male mice with another 4 weeks CCl₄/olive oil treatment). Total liver cells (including parenchymal and non-parenchymal cells) were harvested 48 h after i.v. administration of mCre LNP formulations (1.5 mg/kg). Parenchymal cells, specifically primary hepatocytes were harvested by perfusion method as described above. Non-parenchymal cells (including endothelial, HSCs, leucocytes) were harvested in the supernatant. Cell types were distinguished by size and specific markers by flow cytometry (Hepatocytes: low SSC/HSC, CD45⁻; Endothelial: CD45⁻, CD31⁺; Leucocytes, CD45⁺; other cells (mainly HSCs)). The percentage of tdTomato⁺ cells in each cell populations were measured and quantified.

Pharmacokinetics assay

The liver fibrosis models were developed using 8-week-old male C57BL/6J mice with another 4 weeks CCl₄/olive oil treatment. The fibrotic mice were i.v. treated with ATRA LNPs containing mRLN, mRLN-PLGF₁, mRLN-PLGF₃ and mRLN-Fc at a concentration of 1.5 mg/kg. At 0.25, 1, 3, and 6 days post injection, and both liver tissue and blood samples were harvested. The RLN content in the samples was determined using an ELISA kit (Boster bio) following the manufacturer's protocol.

Efficacy study

CCl₄-induced liver fibrosis models (4 weeks) in 8-week-old male C57BL/6J mice were developed as previously described. At day 0, 3, 6, and 9,

the mice were i.v. treated with PBS, ATRA LNPs containing mRLN, mRLN-PLGF₁, mRLN-PLGF₃, and mRLN-Fc at a concentration of 1.5 mg/kg, and Blank ATRA LNPs with the same lipid concentration. For OCA group, mice were dosed with OCA solution at a concentration of 10 mg/kg through oral gavage. On the third day after the last administration, the mice were euthanized by CO₂ inhalation. The blood and main organs (heart, liver, spleen, lung and kidney) were collected for tissue slicing and blood chemistry analysis. Furthermore, to evaluate the therapeutic efficiency of IL-10 PLGF₁, the CCl₄-induced liver fibrosis mice were i.v. administrated with PBS, ATRA LNPs containing mIL10 and mIL10-PLGF₁ with a concentration of 1.5 mg/kg at day 0, 3, 6, and 9. On the third day after the last administration, the blood and liver were collected for blood chemistry analysis, tissue slicing, and ELISA assay.

MCD models (8 weeks) in C57BL/6J mice were developed as previously described. At day 0, 5, and 10, the mice were i.v. treated with PBS, ATRA LNPs containing mRLN and mRLN-PLGF₁ with a concentration of 1.5 mg/kg. On the third day after the last administration, the blood and liver were collected for tissue slicing and blood chemistry analysis.

CDHFD-induced MASH hamster models were developed as previously described. ATRA LNP formulated mRLN-PLGF₁ and mIL-10-PLGF₁ were administrated through jugular vein at a concentration of 1.5 mg/kg for mono-dose regimen or 0.75 mg/kg each for combination. Hamsters on CDHFD with sham surgery in the jugular vein were served as a control. In vivo ultrasound imaging of livers from the CDHFD-induced MASH hamsters were carried out for all treatment groups at 0, 6, 12 and 18 d post the first dose treatment (Vevo 3100 LAZR with Vevo lab instrument, FUJIFILM VisualSonics, Canada). Blood was collected from MASH hamsters and serum lipid level (TG and TC) and ALT and AST were measured for all treatment groups at 0, 6, 12, 18 d post the first dose treatment. At 18 d post the first dose treatment, blood and main organs (heart, liver, spleen, lung, and kidney) were collected for tissue slicing, blood chemistry analysis, and qPCR assay.

Blood chemistry analysis

Serum was collected by 4500 × g centrifugation of whole blood at 4 °C for 15 min. Transaminase (ALT and AST) and lipid profile (total cholesterol and triglycerides) were determined using corresponding kits (Jiancheng, Nanjing) on Biotek Synergy H1 microplate reader with Gen5 3.11 software.

Biosafety evaluation

Healthy ICR mice (male, 8 weeks old) were intravenously administered with mPLGF₁-RLN LNP at doses of 0, 0.75, 1.5, 3 and 5 mg/kg for single dose and triple doses with an interval of 3 days. On the next day after single dose and 3 days after triple doses, the serum was collected for hepatic and renal function measurements. Then major organs including heart, liver, spleen, lung, and kidney were also harvested 3 days after dose 3 to evaluate the pathological changes through H&E stainings.

Isolation of primary hepatocytes

Mouse primary hepatocytes were isolated from 8-week-old male C57BL6/J mice using a well-established two-step collagenase perfusion technique.¹ In brief, the liver was washed and perfused with collagenase IV (Sigma) via hepatic portal vein to dissociate ECM. Then, liver was dissected, dissociated, and centrifuged at low-speed (50 × g for 2 min, 3–4 times) to isolate hepatocytes. The purified hepatocytes were plated on 96-well plates precoated with rat tail collagen I (Solarbio, China) in Dulbecco's modified Eagle's medium (DMEM, Meilunbio, China) supplemented with penicillin, streptomycin, and fetal bovine serum (Procell, China). To achieve lipid-overloaded hepatocytes, the freshly isolated hepatocytes were incubated with DMEM containing 1% bovine serum albumin (BSA) and 0.5 mM oleic

acid for 16 h. Lipid-loading was visualized by oil-red staining following manufacturer's protocols.

Endosome isolation and characterization

Cells in culture were collected by centrifugation (850 × g, 2 min, 4 °C). Tissues were minced into small pieces, and subsequently homogenized using Dounce Homogenizer on ice. Cell lysis and organelles were then removed using lysosome enrichment kit according to the manufacturers' protocol. Endosome was further isolated by density gradient centrifugation for 145,000 × g, 2 h at 4 °C. The collected endosomes were washed three times and characterized using western blotting with Rab-5, the biomarkers of endosome (Cell Signaling Technology). The isolated organelles were gone through lipidomics (Supplementary Methods).

Lipidomics

Overall design of study. In our study, non-targeted metabolomics was conducted using Vanquish ultra-high performance liquid chromatography-tandem Mass Spectrometry (UHPLC-MS/MS) analysis. The samples were injected into Vanquish UHPLC system (Thermo Fisher, Germany) and detected using Orbitrap Q Exactive TM HF mass spectrometer (Thermo Fisher, Germany) with Electrospray ionization (ESI) source. The schematic diagram of overall design of the lipidomic study is shown in Supplementary Fig. 37. More detail information was described in sections b–g.

Sample preparation and lipid extraction. Endosomes from activated fibroblasts and primary hepatocytes were isolated using lysosome enrichment kit followed by density gradient centrifugation according to the manufacturers' protocol (ThermoFisher Co. Ltd). Samples were parallel triplets for each group (from 3 biological independent mice for primary hepatocytes). The weight of the isolated endosome was used for sample normalization. For lipid extraction, a methyl tert-butyl ether (MTBE) based liquid-liquid extraction method was employed^{48,53–55}. Briefly, methanol (0.75 mL) was added to a glass tube containing 100 mg of the sample, which was then vortexed to ensure thorough mixing. Then 2.5 mL of MTBE was added and the mixture was incubated for 1 h at room temperature. Phase separation was induced by adding 0.625 mL water to the mixture. Upon 10 min of incubation at room temperature, the sample was centrifuged at 1000 × g for 10 min. The upper (organic) phase containing the extracted lipids was collected, and the lower phase was re-extracted with 1 mL of the solvent mixture (MTBE/methanol/water (10:3:2.5, v/v/v)). The combined organic phases were dried and dissolved in 100 μL of isopropanol for storage. During LC-MS/MS analysis, five μL of each sample was injected to ensure sample normalization. The isopropanol supernatant from each processed sample was mixed in equal amounts, and the resulting mixture was divided into three quality control (QC) aliquots. These QC aliquots were then injected both before and after the test samples. The order for sample preparation and data collection of biological samples was randomized.

UHPLC-MS/MS analysis. Samples were injected onto a Thermo Accucore C30 column (150 × 2.1 mm, 2.6 μm) using a 20-min linear gradient at a flow rate of 0.35 mL/min. The column temperature was set at 40 °C. Mobile phase buffer A was acetonitrile/water (6/4) with 10 mM ammonium acetate and 0.1% formic acid, whereas buffer B was acetonitrile/ isopropanol (1/9) with 10 mM ammonium acetate and 0.1% formic acid. The solvent gradient was set as follows: 30% B, initial; 30% B, 2 min; 43% B, 5 min; 55% B, 5.1 min; 70% B, 11 min; 99% B, 16 min; 30% B, 18.1 min. Q Exactive TM HF Orbitrap mass spectrometer with ESI and full scan was operated in positive/negative polarity with data-dependent acquisition scan mode and resolution of 120,000 full width at half maximum. Other parameters are set as follows: sheath gas:40 psi, sweep gas: 0 L/min, auxiliary gas rate: 10 L/min/7 L/min, spray

voltage: 3.5 kV, capillary temperature: 320 °C, heater temperature: 350 °C, S-Lens RF level: 50, scan range: 114–1700 m/z , automatic gain control target: 3e6, normalized collision energy: 22 eV; 24 eV; 28 eV, Injection time: 100 ms, Isolation window: 1 m/z , automatic gain control target (MS2): 2e⁵, dynamic exclusion: 6 s.

Lipid identification. The raw data files generated by UHPLC-MS/MS were subjected to data processing using the Lipidsearch software (5.0). This processing involved peak alignment, peak picking, and quantitation for each metabolite. The peaks were matched with the Lipidsearch database using a 5 (parts per million, ppm) actual mass tolerance, 0.05 min retention time tolerance, and a signal-to-noise ratio of 3. K-nearest neighbor classification (kNN) imputation method was applied to fill the missing values. The background response (compounds with peak intensity QCI/blank sample less than 1) was filtered out and compounds with a coefficient of variance (CV) of less than 30% were retained for final identification. For peak extraction, the molecular weight of lipids is determined according to the mass-to-charge ratio (m/z) of the precursor ion in the primary mass spectrometry, and the molecular formula is predicted by mass deviation (ppm) and adduct ions and then matched with the database. We then match the fragment ions, collision energies, and other information of each lipid compound in the database based on the actual secondary spectrum to achieve the secondary identification of lipid compounds. Details of the lipid information were provided in Excel format as Supplementary Data file 2 and 3.

Lipid quantification. The Lipidsearch data processing software was applied to integrate each chromatographic peak detected in samples, where the peak area of represented the relative quantification value of compounds. The quantification results were normalized using the total peak area.

Quality control and method validation. The isopropanol supernatant from each processed sample was mixed in equal amounts, and the resulting mixture was divided into three QC aliquots. These QC aliquots were then injected both before and after the test samples.

Data reporting. The variation of each component from relative quantification was shown as z-score:

$$z = (x - \mu) / \sigma$$

The symbol “ x ” refers to the value of certain components in certain sample; “ μ ” refers to the average of certain components in all samples; “ σ ” represents the standard deviation all samples.

Preparation of polymer-tethered lipid bilayers as cellular membrane mimicking

The artificial model systems were prepared using Langmuir-Blodgett/Langmuir Schaefer (LB/LS) method in a layer-by-layer manner as previously described. In specific, lipid stocks were dissolved in chloroform at 1 mg/ml and spread on top of the air-water interface of a LB trough. After chloroform evaporation, lipids were kept at 30 mN/m in order to keep the lipids at liquid condensed phase. After 30 min, the bottom leaflet was prepared through dipping. The top leaflet was prepared by a similar protocol except the second leaflet was prepared through LS transfer. Compositions of bottom and top leaflets were shown in Supplementary Table 6. The data were collected using Visiview 5 software and analyzed using ImageJ 1.53u.

Quantitative real-time PCR (qPCR) assay

Total RNA of liver tissue and cultured cells were extracted and purified using the TransZol Up Plus RNA Kit (TransGen Biotech). cDNA was reverse-transcribed by HiScript III All-in-one RT SuperMix Perfect for

qPCR (Vazyme Biotech Co., Ltd). qPCR was performed by Sybr green method using qPCR SuperMix (TransGen Biotech) on QuantStudio™ 6 Flex with QuantStudio Real-Time PCR Software v1.7.1. All the primers are listed in Supplementary Fig. S8, in which glyceraldehyde-3-phosphate dehydrogenase (GAPDH) was applied as endogenous control. The quantification was conducted as $2^{-\Delta\Delta Ct}$ value.

Histological and immunofluorescence staining

Hematoxylin and eosin (H&E) staining, Sirius red staining and Masson's trichrome staining were performed on tissue paraffin WS-10 scanner with NDP view 2 (Zhiyue Medical Technology, Hefei) and quantified by Image J 1.53 u. All statistical analysis was performed on 3 different areas in 5 biologically distinct specimens following manufacturer's protocols (Abcam). Oil red O staining was performed on frozen specimens for tissues and cells using saturate Oil Red O solution according to manufacturer's protocol (Meilunbio). All histological staining images were taken by different samples, immunofluorescence staining. The primary and secondary fluorescent antibodies and the corresponding dilution factors are listed in Table S9. Immunofluorescence images were scanned by Vectra Polaris with Phenochart 1.0.8 software (Akoya, USA). Quantification was performed using Image J 1.53 u with the same method as described above.

Statistics and reproducibility

Data are expressed as the mean \pm SEM or mean \pm SD as indicated in each of the figure legend. Statistical significance was determined using a two-tailed unpaired Student's *t*-test when only two value sets were compared or by ANOVA for comparison between multiple groups via GraphPad Prism 9.5. Exact *P* values are documented in the figures or figure legends. Difference was considered to be significant if $P < 0.05$, (* $P < 0.05$, ** $P < 0.01$, *** $P < 0.001$, **** $P < 0.0001$ unless otherwise indicated). For the reproducibility of the results, all the experiments were repeated independently with similar results.

Reporting summary

Further information on research design is available in the Nature Portfolio Reporting Summary linked to this article.

Data availability

All data supporting the findings described in this manuscript are available in the Article, the Supplementary Information and from the corresponding author upon request. All data have been deposited in the Figshare database (<https://figshare.com/s/478747889070c5f8c823>). Raw files associated with the lipidomics study have been deposited in the Metabolights database (www.ebi.ac.uk/metabolights/MTBLS9132). A reporting summary for this article is available as a Supplementary Information file.

Code availability

Related source codes for generating data in Fig. 3o are available on the GitHub repository: (<https://github.com/miaolabpku/fort/blob/main/fort.ipynb>).

References

- Huby, T. & Gautier, E. L. Immune cell-mediated features of non-alcoholic steatohepatitis. *Nat. Rev. Immunol.* **22**, 429–443 (2022).
- Musso, G., Cassader, M. & Gambino, R. Non-alcoholic steatohepatitis: emerging molecular targets and therapeutic strategies. *Nat. Rev. Drug Discov.* **15**, 249–274 (2016).
- Dufour, J. F., Caussy, C. & Loomba, R. Combination therapy for non-alcoholic steatohepatitis: rationale, opportunities and challenges. *Gut* **69**, 1877–1884 (2020).
- Yang, T. et al. Therapeutic HNF4A mRNA attenuates liver fibrosis in a preclinical model. *J. Hepatol.* **75**, 1420–1433 (2021).

5. Rizvi, F. et al. Murine liver repair via transient activation of regenerative pathways in hepatocytes using lipid nanoparticle-complexed nucleoside-modified mRNA. *Nat. Commun.* **12**, 613 (2021).
6. Hu, M. et al. Hepatic macrophages act as a central hub for relaxin-mediated alleviation of liver fibrosis. *Nat. Nanotechnol.* **16**, 466–477 (2021).
7. Devarakonda, T. et al. B7-33, a functionally selective relaxin receptor 1 agonist, attenuates myocardial infarction-related adverse cardiac remodeling in mice. *J. Am. Heart Assoc.* **9**, e015748 (2020).
8. Sun, J. et al. Human relaxin-2 fusion protein treatment prevents and reverses isoproterenol-induced hypertrophy and fibrosis in mouse heart. *J. Am. Heart Assoc.* **8**, e013465 (2019).
9. Hossain, M. A. et al. Development of novel high-affinity antagonists for the relaxin family peptide receptor 1. *ACS Pharm. Transl. Sci.* **6**, 842–853 (2023).
10. Nga, H. T. et al. Interleukin-10 attenuates liver fibrosis exacerbated by thermoneutrality. *Front. Med.* **8**, 672658 (2021).
11. Zhang, B. et al. Site-specific PEGylation of interleukin-2 enhances immunosuppression via the sustained activation of regulatory T cells. *Nat. Biomed. Eng.* **5**, 1288–1305 (2021).
12. Astrup, A. et al. Effects of liraglutide in the treatment of obesity: a randomised, double-blind, placebo-controlled study. *Lancet* **374**, 1606–1616 (2009).
13. Mansurov, A. et al. Collagen-binding IL-12 enhances tumour inflammation and drives the complete remission of established immunologically cold mouse tumours. *Nat. Biomed. Eng.* **4**, 531–543 (2020).
14. Martino, M. et al. Growth factors engineered for super-affinity to the extracellular matrix enhance tissue healing. *Science* **343**, 885–888 (2014).
15. Bracho-Sanchez, E. et al. Suppression of local inflammation via galectin-anchored indoleamine 2,3-dioxygenase. *Nat. Biomed. Eng.* **7**, 1156–1169 (2023).
16. Davies, N. et al. Functionalized lipid nanoparticles for subcutaneous administration of mRNA to achieve systemic exposures of a therapeutic protein. *Mol. Ther. Nucl. Acids* **24**, 369–384 (2021).
17. Cheng, Q. et al. Selective organ targeting (SORT) nanoparticles for tissue-specific mRNA delivery and CRISPR-Cas gene editing. *Nat. Nanotechnol.* **15**, 313–320 (2020).
18. Zhang, Y. et al. Close the cancer-immunity cycle by integrating lipid nanoparticle-mRNA formulations and dendritic cell therapy. *Nat. Nanotechnol.* **18**, 1364–1374 (2023).
19. Lee, J., Byun, J., Shim, G. & Oh, Y. K. Fibroblast activation protein activated antifibrotic peptide delivery attenuates fibrosis in mouse models of liver fibrosis. *Nat. Commun.* **13**, 1516 (2022).
20. Sato, Y. et al. Resolution of liver cirrhosis using vitamin A-coupled liposomes to deliver siRNA against a collagen-specific chaperone. *Nat. Biotechnol.* **26**, 431–442 (2008).
21. Katsumata, K. et al. Conferring extracellular matrix affinity enhances local therapeutic efficacy of anti-TNF- α antibody in a murine model of rheumatoid arthritis. *Arthritis Res. Ther.* **21**, 298 (2019).
22. Seo, Y. et al. Recent progress of lipid nanoparticles-based lipophilic drug delivery: focus on surface modifications. *Pharmaceutics* **15**, 772 (2023).
23. Blaner, W. S. et al. Hepatic stellate cell lipid droplets: a specialized lipid droplet for retinoid storage. *BBA Mol. Cell Biol. L* **1791**, 467–473 (2009).
24. Gudas, L. J. Synthetic retinoids beyond cancer therapy. *Annu. Rev. Pharmacol. Toxicol.* **62**, 155–175 (2022).
25. Berni, R., Clerici, M., Malpell, G., Cleris, L. & Formelli, F. Retinoids: in vitro interaction with retinol-binding protein and influence on plasma retinol. *FASEB J.* **7**, 6 (1993).
26. Patel, S. et al. Naturally-occurring cholesterol analogues in lipid nanoparticles induce polymorphic shape and enhance intracellular delivery of mRNA. *Nat. Commun.* **11**, 983 (2020).
27. Saeed, A. et al. Impaired hepatic vitamin A metabolism in NAFLD mice leading to vitamin A accumulation in hepatocytes. *Cell. Mol. Gastroenterol. Hepatol.* **11**, 309–325.e303 (2021).
28. Filliol, A. et al. Opposing roles of hepatic stellate cell subpopulations in hepatocarcinogenesis. *Nature* **610**, 356–365 (2022).
29. Mederacke, I., Dapito, D. H., Affò, S., Uchinami, H. & Schwabe, R. F. High-yield and high-purity isolation of hepatic stellate cells from normal and fibrotic mouse livers. *Nat. Protoc.* **10**, 305–315 (2015).
30. Desai, A. S., Hunter, M. R. & Kapustin, A. N. Using macropinocytosis for intracellular delivery of therapeutic nucleic acids to tumour cells. *Philos. Trans. R. Soc. Lond. B Biol. Sci.* **374**, 20180156 (2019).
31. Gilleron, J. et al. Image-based analysis of lipid nanoparticle-mediated siRNA delivery, intracellular trafficking and endosomal escape. *Nat. Biotechnol.* **31**, 638–646 (2013).
32. Viger-Gravel, J. et al. Structure of lipid nanoparticles containing siRNA or mRNA by dynamic nuclear polarization-enhanced NMR spectroscopy. *J. Phys. Chem. B* **122**, 2073–2081 (2018).
33. Ge, Y., Boopathy, S., Smith, A. & Chao, L. H. A model membrane platform for reconstituting mitochondrial membrane dynamics. *J. Vis. Exp.* **163**, e61620 <https://doi.org/10.3791/61620> (2020).
34. Ding, C. et al. Cellular delivery of relaxin-2 mRNA as a potential treatment for kidney fibrosis. *Mater. Today Biol.* **21**, 100716 (2023).
35. Li, Y. J. et al. Delivering relaxin plasmid by polymeric metformin lipid nanoparticles for liver fibrosis treatment. *Curr. Drug Deliv.* **21**, 431–437 (2023).
36. Wahyudi, H., Reynolds, A. A., Li, Y., Owen, S. C. & Yu, S. M. Targeting collagen for diagnostic imaging and therapeutic delivery. *J. Control Release* **240**, 323–331 (2016).
37. Briquez, P. S., Tsai, H. M., Watkins, E. A. & Hubbell, J. A. Engineered bridge protein with dual affinity for bone morphogenetic protein-2 and collagen enhances bone regeneration for spinal fusion. *Sci. Adv.* **7**, eabh4302 (2021).
38. Ishihara, J. et al. The heparin binding domain of von Willebrand factor binds to growth factors and promotes angiogenesis in wound healing. *Blood* **133**, 2559–2569 (2019).
39. Paderi, J. E. & Panitch, A. Design of a synthetic collagen-binding peptidoglycan that modulates collagen fibrillogenesis. *Biomacromolecules* **9**, 2562–2566 (2008).
40. Zhao, W. et al. Vascularization and cellularization of collagen scaffolds incorporated with two different collagen-targeting human basic fibroblast growth factors. *J. Biomed. Mater. Res. A* **82**, 630–636 (2007).
41. Hossain, M. A. et al. A single-chain derivative of the relaxin hormone is a functionally selective agonist of the G protein-coupled receptor, RXFP1. *Chem. Sci.* **7**, 3805–3819 (2016).
42. Hu, M. et al. Relaxin gene delivery mitigates liver metastasis and synergizes with check point therapy. *Nat. Commun.* **10**, 2993 (2019).
43. Marques, A. C., Costa, P. C., Velho, S. & Amaral, M. H. Lipid nanoparticles functionalized with antibodies for anticancer drug therapy. *Pharmaceutics* **15**, 216 (2023).
44. Streiff, S. et al. Primitive” membrane from polypropyl phosphates and polypropyl alcohols. *Chem. Biol.* **14**, 313–319 (2007).
45. Bennett, R. G. Relaxin and its role in the development and treatment of fibrosis. *Transl. Res.* **154**, 1–6 (2009).
46. Unemori, E. Serelaxin in clinical development: past, present and future. *Br. J. Pharmacol.* **174**, 921–932 (2017).
47. Arteta, M. Y. et al. Successful reprogramming of cellular protein production through mRNA delivered by functionalized lipid nanoparticles. *Proc. Natl. Acad. Sci. USA* **115**, E3351–E3360 (2018).
48. Mok, J. H. et al. Optimizing MS-based multi-omics: comparative analysis of protein, metabolite, and lipid extraction techniques. *Metabolites* **14**, 34 (2024).
49. Tomita, K. Tumour necrosis factor signalling through activation of Kupffer cells plays an essential role in liver fibrosis of non-alcoholic steatohepatitis in mice. *Gut* **55**, 415–424 (2006).

50. Yang, C. et al. AAV-mediated ApoC2 gene therapy: reversal of severe hypertriglyceridemia and rescue of neonatal death in ApoC2-deficient hamsters. *Mol. Ther. Methods Clin. Dev.* **18**, 692–701 (2020).
51. Nemmar, A. et al. Ultrafine particles affect experimental thrombosis in an in vivo Hamster model. *Am. J. Respir. Crit. Care Med.* **166**, 998–1004 (2002).
52. Liu, G., Lai, P., Guo, J., Wang, Y. & Xian, X. Genetically-engineered hamster models: applications and perspective in dyslipidemia and atherosclerosis-related cardiovascular disease. *Med. Rev.* **1**, 92–110 (2021).
53. Miranda, A. M. et al. Effects of APOE4 allelic dosage on lipidomic signatures in the entorhinal cortex of aged mice. *Transl. Psychiatry* **12**, 129 <https://doi.org/10.1038/s41398-022-01881-6> (2022).
54. Zhang, J.-J., Cao, D.-Y., Yang, J.-X. & Shen, K. Ovarian metastasis from nongynecologic primary sites: a retrospective analysis of 177 cases and 13-year experience. *J. Ovarian Res.* **13**, 128 (2020).
55. Kim, Y. B., Lee, G. B. & Moon, M. H. Size separation of exosomes and microvesicles using flow field-flow fractionation/multiangle light scattering and lipidomic comparison. *Anal. Chem.* **94**, 8958–8965 (2022).

Acknowledgements

This research was financially supported by National Key Research and Development Program of China (2023YFC3405000 to L.M.), Beijing Natural Science Foundation (Z220022 to L.M.), Beijing Municipal Science & Technology Commission (Z231100007223012 to L.M.), the National Natural Science Foundation of China (NSFC) grants (HY2021-8, 82373807 to L.M., 82070460, 82270479, HY2021-1 to X.D.X., 32350018 to Y.F.G.), the Youth Innovation Promotion Association, Chinese Academy of Sciences (Grant 2020010 to Y.B.K.). We thank the State Key Laboratory of Natural and Biomimetic Drugs, Peking University Biological Imaging Facility for confocal, animal, and tissue imaging services. The molecular modelling and dynamics simulations were carried out using the high-performance Linux cluster at the Computing and Data Science Core in the Chinese Institute for Brain Research, Beijing. We thank Keymed Biosciences for providing related proteins. We thank Proxybio Therapeutics for providing related mRNAs.

Author contributions

L.M., X.Z.S., and Z.Q.Z. are responsible for all phases of the research. X.Z.S., Z.Q.Z., P.P.L., B.Y.L., P.X.Q., Y.Z.X., Z.H.Z., C.L.W. and B.M. performed experiments. Y.B.K. and H.Q.J. helped with SANS experiment. W.L. provided purified fusion proteins and cell lysates. W.Z.L. helped with cell uptake and confocal analysis. Q.W. participated in SPR and MST assay. J.Y. and Y.X.L. performed the molecular modeling and dynamics simulation of fusion proteins. Y.F.G. and L.S. performed the lipid

membrane simulation. X.Z.S., Z.Q.Z., and L.M. wrote the manuscript. C.L., Y.L.Z., X.G.L., J.Q.L., X.D.X., D.D., and L.M. provided conceptual advice and supervised the study. All the authors discussed the results and assisted in the preparation of the manuscript.

Competing interests

M, X.Z.S., Z.Q.Z. have filed a patent for the development of the described FORT strategy. The remaining authors declare no competing interests.

Additional information

Supplementary information The online version contains supplementary material available at <https://doi.org/10.1038/s41467-024-51571-8>.

Correspondence and requests for materials should be addressed to Lei Miao.

Peer review information *Nature Communications* thanks Hideyoshi Harashima, Klaas Poelstra, Mahmoud Younis and the other anonymous reviewer(s) for their contribution to the peer review of this work. A peer review file is available.

Reprints and permissions information is available at <http://www.nature.com/reprints>

Publisher's note Springer Nature remains neutral with regard to jurisdictional claims in published maps and institutional affiliations.

Open Access This article is licensed under a Creative Commons Attribution-NonCommercial-NoDerivatives 4.0 International License, which permits any non-commercial use, sharing, distribution and reproduction in any medium or format, as long as you give appropriate credit to the original author(s) and the source, provide a link to the Creative Commons licence, and indicate if you modified the licensed material. You do not have permission under this licence to share adapted material derived from this article or parts of it. The images or other third party material in this article are included in the article's Creative Commons licence, unless indicated otherwise in a credit line to the material. If material is not included in the article's Creative Commons licence and your intended use is not permitted by statutory regulation or exceeds the permitted use, you will need to obtain permission directly from the copyright holder. To view a copy of this licence, visit <http://creativecommons.org/licenses/by-nc-nd/4.0/>.

© The Author(s) 2024